A finite volume framework for the fully implicit thermal-hydro-mechanical-compositional modeling in subsurface applications

Novikov, Aleksei; Saifullin, Ilshat; Hajibeygi, Hadi; Voskov, Denis

Important note
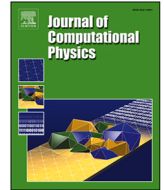To cite this publication, please use the final published version (if applicable).
Please check the document version above.

A finite volume framework for the fully implicit thermal-hydro-mechanical-compositional modeling in subsurface applications

Aleksei Novikov [a,*], Ilshat Saifullin [a], Hadi Hajibeygi [a], Denis Voskov [a,b]

a *Faculty of Civil Engineering and Geosciences, Delft University of Technology, Stevinweg 1, Delft, 2628 CN, the Netherlands*
b *Department of Energy Science and Engineering, Stanford University, 367 Panama Street, Stanford, 94305, CA, USA*

ARTICLE INFO

ABSTRACT

Thermal-Hydro-Mechanical-Compositional analysis is crucial for addressing challenges like wellbore stability, land subsidence, and induced seismicity in the geo-energy applications. Numerical simulations of coupled thermo-poromechanical processes provide a general-purpose tool for evaluating these phenomena across laboratory and field scales. However, efficient integration of the coupled equations for fluid mass, energy and momentum poses multiple numerical and implementation difficulties, such as combining different numerical methods on staggered grids and associated limitations on admissible grids. This paper introduces a novel fully-implicit Finite Volume Method (FVM) for modeling thermal compositional flow in thermo-poroelastic rocks. The scheme employs gradient-based, coupled multi-point approximations of fluid mass, momentum and heat fluxes.

The novelty of the scheme lies in its integration of temperature as a parameter in the flux approximation process. The scheme supports a wide range of cell topologies, arbitrary heterogeneity and anisotropy as well as various boundary conditions, while respecting local flux balance under temperature gradients. Overall, the scheme represents a unified FVM-based approach for the integration of all conservation laws relevant to geo-energy applications on a cell-centered collocated grid. Additionally, the implemented two-stage block-partitioned preconditioning strategy enables the efficient solution of obtained linear systems.

The framework, implemented in the open-source Delft Advanced Research Terra Simulator (open-DARTS), leverages the Operator-Based Linearization (OBL) technique for flexibility in compositional fluid properties. Rigorous validation demonstrates the framework's capabilities in capturing advanced phenomena, including thermal expansion, thermo-poroelastic effect and compositional flow with phase transitions. The performance of preconditioning strategy is assessed using the mechanical extension of the SPE10 benchmark model.

1. Introduction

Geomechanics is crucial for the safe and optimal operation of modern geo-energy applications [1]. Changes in subsurface condition, such as pressure depletion during gas production, can cause subsidence, initiate induced seismicity, and result in serious damage to

Nomenclature

Physical variables

$\mathbf{A}$	rank-two rock thermal dilation tensor,
α_ϕ	volumetric thermal dilation coefficient related to porosity
$\mathbf{B}$	rank-two Biot tensor,
$\mathbb{C}$	rank-four stiffness tensor of skeleton,
$\mathbf{C}$	6×6 matrix of stiffness coefficients,
c_α	heat capacity of fluid phase α,
c_s	rock heat capacity,
D	depth,
$\boldsymbol{\varepsilon}$	rank-two infinitesimal strain tensor,
E	Young's modulus,
$\mathbf{f}$	traction vector,
$f_N, \mathbf{f}_T$	normal and tangential projections of traction vector,
G	specific (molar) Gibbs energy of fluid mixture,
g	gravity constant,
h_α	enthalpy of phase α,
$\mathbf{I}$	identity matrix,
$\mathbf{K}$	rank-two tensor of permeability,
k_x, k_y, k_z	diagonal components of permeability tensor,
$k_{r\alpha}$	relative permeability of fluid phase f,
K_r	bulk modulus of the solid phase,
$\boldsymbol{\Lambda}$	rank-two effective heat conductivity tensor,
μ_α	fluid viscosity of fluid phase α,
$\mathbf{n}$	unit normal vector,
ν	Poisson's ratio,
p	pore pressure,
$\mathbf{q}_\alpha^f$	Darcy's velocity of fluid phase f,
$\mathbf{q}_\alpha^\theta$	heat conduction vector fluid constituent α (fluid phase of rock),
r_α	sources (or sinks) of fluid mass of phase α,
ρ_α	density of constituent α,
R	gas constant,
S_α	saturation of fluid phase α,
$\boldsymbol{\sigma}$	rank-two total stress tensor,
Θ	temperature,
t	time,
U_f	fluid internal energy,
U_r	rock internal energy,
$\mathbf{u} = \begin{bmatrix} u_x\, u_y\, u_z \end{bmatrix}^T$	vector of displacements,
$(\nabla\mathbf{u})^T$	Jacobian matrix of $\mathbf{u}$,
$\varphi_{i\alpha}$	fugacity of component i in phase α,
ϕ	porosity,
$\tilde{\phi} = \phi_0 +$ $(p - p_0)(\psi - \phi_0)/K_r$,	
$\psi = (\mathbf{B} : \mathbf{I})\,/\,3$	one-third of the trace of tensor $\mathbf{B}$,
x_α	molar fraction of fluid phase α,
$x_{i\alpha}$	molar fraction of component i in fluid phase α,
z_i	overall molar fraction of component i.

Numerical variables

Δt	time step,
δ_j	area of jth interface,
$\mathbf{H}$	vector of residuals,
$\mathbf{J}$	Jacobian matrix,
$\boldsymbol{\delta p}$	unknown increments of pressures,
$\boldsymbol{\delta z}$	unknown increments of compositions (and temperatures for non-isothermal systems),
$\boldsymbol{\delta u}$	unknown increments of displacements,
$\boldsymbol{\omega} = \{p, \mathbf{z}_i, \Theta\}$	vector of state unknowns.

surface infrastructures [2,3]. In geothermal operations, the re-injection of cooler fluid causes stress and strain changes that can potentially (re-)activate faults and lead to induced seismic activity [4,5]. The development of CO_2 geological storage involves a complex interaction of thermal, hydraulic, mechanical, and chemical processes which collectively change the in-situ stress state, affect fault stability, and can lead to fault activation, CO_2 leakage and seismicity [6,7]. Therefore, the successful and risk-free exploitation of subsurface resources depends on the development of robust and efficient computational techniques for modeling the coupled geomechanics and hydrothermal processes.

The Finite Volume Method (FVM) has recently been seen as a promising technique for modeling of geomechanics, especially when mechanical interactions are modeled in a fully coupled manner with the flow and transport of mass and energy. The FVM is attractive because it represents an integral form of conservation laws. Recent literature highlights its development for geomechanical simulations with both staggered [8–10] and collocated grids [11–13]. The advantages of FVM include support of various cell topologies, respect of local flux balance, discontinuous representation of displacements, and seamless integration with fluid mass and energy balance solvers.

The first FVM for solid mechanics was limited to homogeneous isotropic elasticity [14]. However, geological formations often exhibit heterogeneity amplified by material discontinuities which require appropriate treatment by numerical scheme. To address this limitation, the multi-point stress approximation (MPSA) has been introduced by [11]. Nevertheless, on simplex meshes, MPSA requires enforcement of continuity at multiple points and, eventually, struggle to maintain convergence. Later, these problems have been resolved by the weakly imposed symmetry of stress tensor [15]. Alternatively, a gradient-based approach allows these complications to be circumvented by offering robust convergence across a wide range of star-shaped topologies [12]. This method relies on the suitable approximations of gradients of unknowns avoiding the excessive construction of dual grid. Later, this approach has been extended to poroelasticity [16], with frictional contact [13] and the Navier-Stokes equations [17]. In this paper, we further extend this gradient-based approach to thermo-poroelastic media.

Coupling fluid flow and mechanics equations poses significant challenges and two well-known approaches can be mentioned. The first approach, sequential implicit (SI), decouples the mechanics and flow equations, achieving a converged solution for the coupled problem by sequentially iterating between subproblems [18,19]. A prominent example of SI approach is the fixed-stress splitting algorithm [20,21]. In contrast, the fully implicit (FI) approach involves a monolithic solution of the coupled system of equations [9,22], offering the advantage of unconditional stability under appropriate assumptions [19]. Nevertheless, FI requires scalable preconditioners specifically designed for solving associated linear systems [23]. Beyond the computational challenges, both approaches are susceptible to inf-sup instabilities, which arise from the saddle-point nature of the displacement-pressure system [24,25]. These instabilities can introduce unphysical oscillations to numerical solution in the limit of undrained conditions [26–29]. The collocated scheme of FVM presented in this paper is not an exception [13,16]. The schemes of FVM are reportedly stabilized by the use of essentially inf-sup-stable discretization spaces [30] and flux vector splitting [31], although the latter one can introduce significant diffusion [32]. We leave the inf-sup stabilization and related analysis beyond the scope of the current paper.

Although the FI approach does not impose any restriction on time step size, it requires efficient nonlinear and linear solution strategies for high-resolution models. One such strategy is to construct a preconditioner based on the idea of the SI approach. In [33], the authors employ a fixed-stress splitting concept in a sparse approximation of the Schur complement to obtain a block-preconditioned solution strategy. Later this approach was combined with a constrained pressure residual (CPR) preconditioner to construct a robust and effective solution strategy for coupled multiphase flow and mechanics [23,34].

In this study, we present a novel cell-centered collocated FI multi-point FVM scheme for thermo-hydro-mechanical-compositional simulation of subsurface reservoirs. It treats mass, energy, and momentum fluxes in a unified vector form within the framework of FVM, resulting in a simplified formulation. The framework can be used to resolve the coupled processes in arbitrarily anisotropic thermoporoelastic rocks on unstructured polyhedral grids with a minimum number of degrees of freedom per cell. It is also capable of handling material heterogeneities while preserving mass, energy and momentum balances. The framework supports multiphase compositional fluid physics, including phase equilibrium and chemical reactions resolved through operator-based linearization [35]. To improve the performance of simulation, a block-partitioned preconditioning strategy is implemented. The developed computational capabilities are verified in benchmarks and demonstrated for compositional modeling using a geomechanical extension of SPE10 model [19].

The developed methods are implemented in the open-source Delft Advanced Research Terra Simulator (open-DARTS) [36]. Open-DARTS is a scalable parallel simulator, which has been successfully applied for modeling of hydrocarbon [37,38], geothermal [39,40], CO_2 sequestration [41,42] applications, as well as evaluating potential to fault reactivation and seismicity [13,32]. This study further extends the coupling between geomechanical modeling and the advanced hydro-thermal modeling capabilities of open-DARTS, making it a fully coupled thermo-hydro-mechanical-compositional simulator for complex geo-energy applications.

2. Governing equations

2.1. Continuous formulation

We employ a displacement-based formulation of a quasi-static linear momentum balance and molar-based formulation for multiphase multicomponent fluid flow in thermo-poroelastic saturated media. Thus, considering a finite domain $\Omega \subset \mathbb{R}^3$ surrounded by a piecewise-smooth boundary $\partial\Omega$ and a time interval $\mathcal{I} = \left[0, t_{\max}\right]$, the primary unknowns include pore pressure $p : \Omega \times \mathcal{I} \to \mathbb{R}$, $n_c - 1$ component molar fractions $z_i : \Omega \times \mathcal{I} \to \mathbb{R}$, temperature $\Theta : \Omega \times \mathcal{I} \to \mathbb{R}$ and vector of displacement $\mathbf{u} : \Omega \times \mathcal{I} \to \mathbb{R}^3$. All unknowns

belongs to Sobolev space $H^1(\Omega)$ with appropriate amendment at $\partial\Omega$. In the region $\Omega \times \mathcal{I}$, we study the mass balances of fluid components $i = 1, \ldots, n_c$, the energy balance and the momentum balance [43] that can be written as

$$\frac{\partial}{\partial t}\left(\phi \sum_{\alpha}^{n_p} x_{i\alpha} S_\alpha \rho_\alpha\right) + \nabla \cdot \left(\sum_{\alpha}^{n_p} x_{i\alpha} \rho_\alpha \mathbf{q}_\alpha^f\right) - \sum_{\alpha}^{n_p} x_{i\alpha} \rho_\alpha r_\alpha = 0, \quad i = 1, \ldots, n_c, \tag{1}$$

$$\frac{\partial}{\partial t}\left((1-\phi)\rho_s U_s + \phi \sum_{\alpha}^{n_p} S_\alpha \rho_\alpha U_\alpha\right) + \nabla \cdot \left(\sum_{\alpha}^{n_p} \left(\rho_\alpha h_\alpha \mathbf{q}_\alpha^f + \phi S_\alpha \mathbf{q}_\alpha^\theta\right) + (1-\phi)\mathbf{q}_s^\theta\right)$$

$$- \sum_{\alpha}^{n_p} \rho_\alpha h_\alpha r_\alpha = 0, \tag{2}$$

$$- \nabla \cdot \boldsymbol{\sigma} - \left((1-\phi)\rho_s + \phi \sum_{\alpha}^{n_p} S_\alpha \rho_\alpha\right) g \nabla D = 0, \tag{3}$$

where subscripts s, α denote rock matrix and fluid phases $1, \ldots, n_p$ respectively, ϕ is porosity, $x_{i\alpha}$ are molar fractions of component i in phase α, S_α are phase saturations, ρ_α are phase densities, $\mathbf{q}_\alpha^f$ are Darcy's phase velocities, r_α are phase source terms, U_s, U_α are the internal energies of rock matrix and fluid phases respectively, h_α are phase enthalpies, $\mathbf{q}_s^\theta$ and $\mathbf{q}_\alpha^\theta$ are the vectors of heat conduction fluxes in rock matrix s and in fluid phase α correspondingly, $\boldsymbol{\sigma}$ is the rank-two total Cauchy's stress tensor, ρ_s is the density of rock matrix, g is the gravitational acceleration, D is depth.

The balance laws in Eqs. (1)–(3) are subjected to the following constitutive relationships [43–45]

$$\mathbf{q}_\alpha^f = -\frac{k_{r\alpha}\mathbf{K}}{\mu_\alpha}\left(\nabla p - \rho_\alpha M_\alpha g \nabla D\right), \tag{4}$$

$$\mathbf{q}_\alpha^\theta = -\boldsymbol{\Lambda}_\alpha \nabla \Theta, \tag{5}$$

$$\phi - \phi_0 = \frac{(\psi - \phi_0)(1-\psi)}{K_s}(p - p_0) + \mathbf{B} : \nabla^s(\mathbf{u} - \mathbf{u}_0) + \alpha_\phi(\Theta - \Theta_0), \tag{6}$$

$$\boldsymbol{\sigma} - \boldsymbol{\sigma}_0 = \mathbb{C} : \nabla^s(\mathbf{u} - \mathbf{u}_0) - (p - p_0)\mathbf{B} - (\Theta - \Theta_0)\mathbf{A}, \tag{7}$$

$$\rho_\alpha = \rho_\alpha(p, \Theta, x_{i\alpha}), \quad \mu_\alpha = \mu_\alpha(p, \Theta, x_{i\alpha}), \quad h_\alpha = c_\alpha(\Theta - \Theta_0), \quad U_\alpha = h_\alpha - \frac{p}{\rho_\alpha}, \tag{8}$$

$$U_s = c_s(\Theta - \Theta_0), \tag{9}$$

$$x_\alpha, x_{i\alpha} = \arg \min_{x_\alpha, x_{i\alpha}} \bar{G}, \quad \bar{G} = \frac{G}{R\Theta} = \sum_{\alpha}^{n_p} x_\alpha \sum_{i}^{n_c} x_{i\alpha} \ln \varphi_{i\alpha},$$

$$z_{i0} = \sum_{\alpha}^{n_p} x_\alpha x_{i\alpha},$$

$$\sum_{\alpha}^{n_p} x_\alpha = \sum_{i}^{n_c} x_{i\alpha} = 1, \quad 0 \le x_\alpha \le 1, \quad 0 \le x_{i\alpha} \le 1, \quad \alpha = 1 \ldots n_p, \quad i = 1 \ldots n_c, \tag{10}$$

where $k_{r\alpha}$ are relative phase permeabilities, $\mathbf{K}$ is the rank-two permeability tensor, p is pore pressure, μ_α are phase viscosities, M_α are phase molar weights, $\boldsymbol{\Lambda}_s$ and $\boldsymbol{\Lambda}_\alpha$ are the rank-two heat conduction tensors of rock matrix and fluid phases respectively, $\nabla^s\mathbf{u} = (\nabla\mathbf{u} + (\nabla\mathbf{u})^T)/2$ is the matrix of symmetric gradients of displacements, $\mathbf{B}$ is the rank-two tensor of Biot's coefficients [43,44,46], $\psi = I_1(\mathbf{B})/3$ is one-third of the first invariant of $\mathbf{B}$, K_s is rock matrix drained bulk modulus, α_ϕ is the volumetric coefficient of rock matrix thermal dilation, $\mathbb{C}$ is the rank-four drained stiffness tensor, $\mathbf{A}$ is the rank-two rock matrix thermal dilation tensor, $\mathbf{u}$ is a vector of displacements, c_s and c_α are constant-pressure heat capacities of rock matrix and fluid phases correspondingly, x_α is molar fraction of phase α, G is the specific (molar) Gibbs energy of fluid mixture, R is gas constant, $\varphi_{i\alpha}$ is the fugacity of component i in phase α, z_{i0} is initial value of overall molar fraction of component i, which must be preserved, and the subscript 0 denotes the reference state of a variable, i.e.,

$$\boldsymbol{\sigma}_0 = \boldsymbol{\sigma}(\mathbf{u}_0, p_0, \Theta_0), \quad \phi_0 = \phi(\mathbf{u}_0, p_0, \Theta_0). \tag{11}$$

Eqs. (4) and (5) represent Darcy's and Fourier's laws that define fluid and heat conduction fluxes caused by spatial variation of pore pressure and temperature respectively, Eqs. (6) and (7) represent porosity and stress changes in anisotropic thermo-poroelastic media under the assumption of infinitesimal strains, the fluid properties, i.e density, viscosity, enthalpy and internal energy are defined in Eq. (8) while rock matrix internal energy is specified in Eq. (9). We employ the multiphase flash [47] to evaluate instantaneous thermodynamic equilibrium between fluid phases written in Eqs. (10). The effect of capillary forces between fluid phases is neglected in both the Darcy's law in Eq. (4) and in the phase equilibrium in Eqs. (10). All variables have been listed in the Nomenclature section at the end of the paper.

The projection of stress tensor $\boldsymbol{\sigma}$ to an interface with unit normal vector $\mathbf{n}$ is called total traction vector $\mathbf{f}$ and defined as

$$\mathbf{f} = -\boldsymbol{\sigma}\mathbf{n}, \tag{12}$$

where the negative sign is motivated by the sign of the corresponding term in the momentum balance in Eq. (3). Traction vector can be decomposed into normal f_N and tangential components $\mathbf{f}_T$ as

$$\mathbf{f} = f_N \mathbf{n} + \mathbf{f}_T, \quad f_N = -\mathbf{n}^T \boldsymbol{\sigma} \mathbf{n}, \quad \mathbf{f}_T = (\mathbf{I} - \mathbf{n}\mathbf{n}^T)\mathbf{f}, \tag{13}$$

where $-f_N$ and $|\mathbf{f}_T|$ are called normal and shear stresses, respectively and $\mathbf{I}$ is an identity matrix.

For the system of balance laws in Eqs. (1)–(3) and constitutive relationships in Eqs. (4)–(10) we consider boundary conditions acting on $\partial\Omega$, which can be written in the following form

$$\alpha_p \mathrm{p}_b + \beta_p \left(\mathbf{K}\mathbf{n} \cdot (\nabla \mathrm{p} - \rho_{\mathrm{f}} \mathrm{g} \nabla D)\right)_b = \gamma_p, \tag{14}$$

$$\alpha_\theta \Theta_b + \beta_\theta (\boldsymbol{\Lambda}\mathbf{n} \cdot \nabla \Theta)_b = \gamma_\theta, \tag{15}$$

$$\mathbf{n}^T \left(\alpha_n \mathbf{u}_b + \beta_n \mathbf{f}_b\right) = \gamma_n, \tag{16}$$

$$(\mathbf{I} - \mathbf{n}\mathbf{n}^T)\left(\alpha_t \mathbf{u}_b + \beta_t \mathbf{f}_b\right) = \boldsymbol{\gamma}_t, \tag{17}$$

where subscript b denotes the property evaluated at the boundary, $\alpha_p, \beta_p, \alpha_\theta, \beta_\theta, \alpha_n, \beta_n$ and α_t, β_t are coefficients that determine the particular kind of boundary conditions, while $\gamma_p, \gamma_\theta, \gamma_n$ and $\boldsymbol{\gamma}_t$ represent the values the corresponding conditions are assigned to, ρ_{f} stands for the effective density of fluid flux estimated as

$$\rho_{\mathrm{f}} = \sum_\alpha^{\mathrm{n}_p} \mathrm{S}_\alpha \rho_\alpha. \tag{18}$$

Additionally, Eq. (14) defines the boundary condition for fluid mass balance, Eq. (15) specifies the boundary condition for energy balance, Eqs. (16), (17) represent normal and tangential boundary conditions for the momentum balance, respectively.

Eqs. (14)–(17) describe a broad range of possible boundary conditions, including fixed boundary for mechanics ($\alpha_n = \alpha_t = 1$, $\beta_n = \beta_t = 0$), distributed force loading ($\alpha_n = \alpha_t = 0$, $\beta_n = \beta_t = 1$), free boundary ($\alpha_n = \alpha_t = \gamma_n = 0$, $\beta_n = \beta_t = 1$, $\boldsymbol{\gamma}_t = \mathbf{0}$) and roller conditions ($\alpha_n = \beta_t = 1$, $\beta_n = \gamma_n = \alpha_t = 0$, $\boldsymbol{\gamma}_t = \mathbf{0}$) for mechanics; Dirichlet ($\alpha_p = \alpha_\theta = 1$, $\beta_p = \beta_\theta = 0$) and Neumann ($\alpha_p = \alpha_\theta = 0$, $\beta_p = \beta_\theta = 1$) conditions for flow and energy.

Eqs. (1)–(3) with substituted Eqs. (4)–(10) represent a system of $\mathrm{n}_c + 4$ equations with respect to primary unknowns: pressure p, $\mathrm{n}_c - 1$ compositions $z_1, \ldots, z_{\mathrm{n}_c-1}$, temperature Θ and three components of displacement vector $\mathbf{u}$. The secondary unknowns defining fluid mixture, e.g. molar fractions $\mathrm{x}_{i\alpha}$ and saturations S_α, are evaluated from primary unknowns inside the multiphase flash procedure. The problem definition is further refined by incorporating boundary conditions as specified in Eqs. (14)–(17), along with the initial values assigned to the unknown variables.

2.2. Discrete formulation

The scheme of FVM for the system of partial differential Eqs. (1)–(3) can be written in the following residual form

$$\mathbf{H}_j^{n+1} = \begin{bmatrix} \mathbf{H}_{m,i} \\ \mathrm{H}_e \\ \mathbf{H}_{mom} \end{bmatrix}_j^{n+1} = j \begin{bmatrix} \mathfrak{a}_i^{n+1} - \mathfrak{a}_i^n - \Delta t_n \mathfrak{r}_i^{n+1} \\ \mathfrak{a}_e^{n+1} - \mathfrak{a}_e^n - \Delta t_n \mathfrak{r}_e^{n+1} \\ \mathfrak{r}_{mom}^{n+1} \end{bmatrix} + \sum_{\beta \in \partial j} \delta_\beta \begin{bmatrix} \Delta t_n \mathfrak{f}_{i,\beta}^{n+1} \\ \Delta t_n \mathfrak{f}_{e,\beta}^{n+1} \\ \mathbf{f}_\beta^{n+1} \end{bmatrix} = \mathbf{0}, \tag{19}$$

where ∂V denotes the set of all interfaces β belonging to cell j, and

$$\mathfrak{a}_i^{n+1} = \left(\phi \sum_\alpha^{\mathrm{n}_p} \mathrm{x}_{i\alpha} \mathrm{S}_\alpha \rho_\alpha \right)_j^{n+1}, \qquad\qquad \mathfrak{r}_i^{n+1} = \left(\sum_\alpha^{\mathrm{n}_p} \mathrm{x}_{i\alpha} \rho_\alpha \mathrm{r}_\alpha \right)_j^{n+1},$$

$$\mathfrak{a}_e^{n+1} = \left((1-\phi)\rho_s \mathrm{U}_s + \phi \sum_\alpha^{\mathrm{n}_p} \rho_\alpha \mathrm{U}_\alpha \right)_j^{n+1}, \qquad \mathfrak{r}_e^{n+1} = \left(\sum_\alpha^{\mathrm{n}_p} \rho_\alpha \mathrm{h}_\alpha \mathrm{r}_\alpha \right)_j^{n+1},$$

$$\mathbf{r}_{mom}^{n+1} = -\left((1-\phi)\rho_s + \phi \sum_\alpha^{\mathrm{n}_p} \mathrm{S}_\alpha \rho_\alpha \right)_j^{n+1} \mathrm{g}\nabla D,$$

$$\mathfrak{f}_{i,\beta}^{n+1} = \sum_\alpha^{\mathrm{n}_p} \left(\left(\mathrm{x}_{i\alpha} \rho_\alpha k_{r\alpha} \mu_\alpha^{-1} \right)_u^{n+1} \mathrm{q}_{\alpha,\beta}^{\mathrm{f},n+1} \right),$$

$$\mathfrak{f}_{e,\beta}^{n+1} = \sum_\alpha^{\mathrm{n}_p} \left((\mathrm{h}_\alpha \rho_\alpha)_u^{n+1} \mathrm{q}_{\alpha,\beta}^{\mathrm{f},n+1} - \phi_j^{n+1} \mathrm{S}_{\alpha,u}^{n+1} \mathrm{q}_{\alpha,\beta}^{\theta,n+1} \right) - (1 - \phi_j^{n+1}) \mathrm{q}_{s,\beta}^{\theta,n+1}.$$

Additionally, $\mathbf{H}_{m,i}$, H_e and $\mathbf{H}_{mom}$ denote the residuals of the mass balances of component i, energy balance and momentum balance respectively, written for cell j; terms $\mathfrak{a}, \mathfrak{r}$ and $\mathfrak{f}$ stand for accumulation, source and flux terms, respectively. Furthermore, j is the volume of a cell j, Δt_n is n-th time step, subscript j denotes the properties evaluated at the center of corresponding cell, subscript β denotes the properties approximated at the center of corresponding interface, subscript u denotes the single-point upstream (SPU) weighting for the interface $\beta = \{j, k\}$ betwee cells j and k

$$\left(\mathrm{x}_{i\alpha} \rho_\alpha k_{r\alpha} \mu_\alpha^{-1} \right)_u = \begin{cases} \left(\mathrm{x}_{i\alpha} \rho_\alpha k_{r\alpha} \mu_\alpha^{-1} \right)_j, & \mathrm{q}_{\alpha,\beta}^{\mathrm{f}} > 0, \\ \left(\mathrm{x}_{i\alpha} \rho_\alpha k_{r\alpha} \mu_\alpha^{-1} \right)_k, & \mathrm{q}_{\alpha,\beta}^{\mathrm{f}} \leq 0, \end{cases} \tag{20}$$

supercripts n and $n + 1$ denote the current and the next time layers respectively, δ_β is the surface area of interface β. Besides, we use the following notations

$$q^f_{\alpha,\beta} = -\left(\mathbf{K}\mathbf{n}\cdot(\nabla p - \rho_\alpha g\nabla D)\right)_\beta, \quad q^\theta_\beta = -(\boldsymbol{\Lambda}\mathbf{n}\cdot\nabla\Theta)_\beta, \tag{21}$$

where q^f_α is the Darcy's flux from Eq. (4), q^θ_α is the Fourier's heat conduction flux from Eq. (5).

Moreover, we approximate porosity defined in Eq. (6) as

$$\phi^{n+1}_j = \left[\phi_0 + \frac{(\psi - \phi_0)(1-\psi)}{K_s}(p - p_0) + \alpha_\phi(\Theta - \Theta_0)\right]^{n+1}_j + \frac{1}{j}\sum_{\beta\in\partial j}\delta_\beta\left(\tilde{q}^{n+1}_\beta - \tilde{q}^n_\beta\right). \tag{22}$$

where the flux $\tilde{q}_\beta$ is defined as

$$\tilde{q}_\beta = \left(\mathbf{u}_\beta - \mathbf{u}_j\right)\cdot(\mathbf{B}\mathbf{n})_j. \tag{23}$$

Note that $\mathbf{u}_j$ will vanish upon summation over the interfaces in Eq. (22), but we retain it here for clarity.
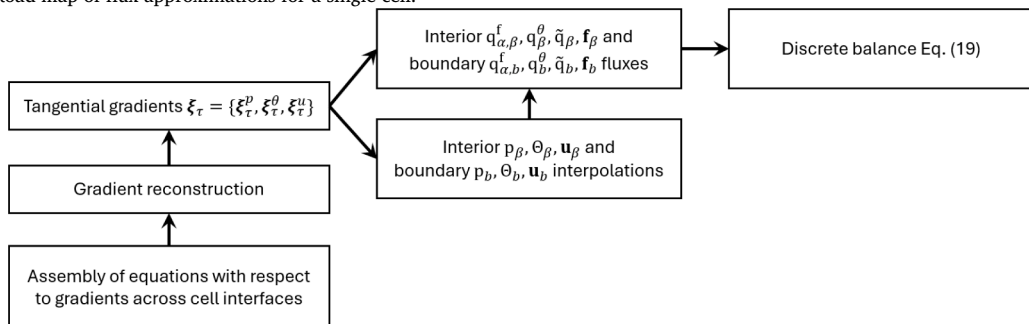
2.3. Approximation of fluxes

Many numerical schemes of FVM rely on flux approximation. Widely exploited in reservoir engineering, the Two-Point Flux Approximation (TPFA) is applicable for diffusive fluxes under certain constraints. Recently, the Two-Point Stress Approximation (TPSA) was introduced as a method to approximate fluxes in the micropolar elasticity formulation using only two points, though it also remains subject to restrictions on admissible meshes [48]. The Multi-Point Flux Approximation (MPFA) [49,50] is not limited by those constraints but can introduce instability [51]. Its extension to momentum fluxes in elasticity systems is called Multi-Point Stress Approximation [11], which has been combined into the MPFA-MPSA approach for the coupled modeling of poroelasticity [30] and thermoporoelasticity [52,53] systems. To improve the stability properties of multi-point schemes, a family of weighted schemes has been developed [54] resulting in the evolution of nonlinear FVM schemes [55–57].

In this work, we extend the gradient-based weighted scheme initially proposed for poroelasticity systems [16], to thermoporoelasticity systems. Specifically, we utilize MPFA for heat conduction fluxes and the associated interpolation of temperature at the interface for the approximation of thermally-induced traction components. This interpolation incorporates temperature into the local balance of total traction vectors, resulting in the temperature-dependent displacement gradient approximation. This methodology follows the coupled scheme construction for poroelasticity systems [16]. Additionally, we apply single-point upstream weighting for the mobility multipliers in mass and heat convection fluxes.

Our gradient-based weighted multi-point approximations rely on reconstruction of the gradients of the unknowns. Specifically, reconstructed gradients are substituted into the flux expressions, with gradient approximations computed before simulation. Following the original scheme's development [16], we manually resolve the gradient components normal to the interface, retaining only the tangential components for reconstruction. This splitting is motivated by the improved behavior of the resulted flux approximation in regard to the locking issue [58]. Once gradients are reconstructed within each cell, facial approximations use arithmetic weighting between neighboring cells.

The following subsections detail the approximations of fluid mass, heat and momentum fluxes (tractions), facial interpolations of pressure, temperature, and displacements for both interior and boundary interfaces, required for the assembly of system in Eq. (19). These approximations are based on the reconstruction of gradients of the unknowns, with a single gradient per cell evaluated from the continuity constraints on fluxes and unknowns across all cell interfaces. The continuity constraints for interior and boundary interfaces, along with flux approximations, are presented in the respective subsections. The final assembly of cell gradients, used in the flux approximations, is described in Section 2.3.3. The complete road map of flux approximations is depicted in Table 1.

Table 1
Road map of flux approximations for a single cell.

2.3.1. Approximation of fluxes at interior interfaces

The approximation of fluxes can be derived from the continuity of unknowns $\mathbf{d} = \begin{bmatrix} p, \Theta, \mathbf{u}^T \end{bmatrix}$ and associated fluxes. Assuming piecewise-linear $\mathbf{d}$ and piecewise-constant $\mathbf{K}, \mathbf{\Lambda}, \mathbb{C}, \mathbf{B}, \mathbf{A}$ defined on a given partitioning of Ω, we enforce the continuity of Darcy's, heat conduction and momentum fluxes (traction vectors), along with the continuity of unknowns. These constitute the local problem – a set of fundamental premises enforced at each interface. For an interior interface with unit normal vector $\mathbf{n}$ between cells 1 and 2, the local problem is expressed as:

$$\mathbf{d}_{\beta 1} = \mathbf{d}_1 + \left[\mathbf{I} \otimes (\mathbf{x}_\beta - \mathbf{x}_1)^T \right] (\nabla \otimes \mathbf{d}_1) = \mathbf{d}_2 + \left[\mathbf{I} \otimes (\mathbf{x}_\beta - \mathbf{x}_2)^T \right] (\nabla \otimes \mathbf{d}_2) = \mathbf{d}_{\beta 2}, \tag{24}$$

$$-\left(\nabla p_1 - \rho_f g \nabla D \right) \cdot \mathbf{K}_1 \mathbf{n} = -\left(\nabla p_2 - \rho_f g \nabla D \right) \cdot \mathbf{K}_2 \mathbf{n}, \tag{25}$$

$$-\nabla \Theta_1 \cdot \mathbf{\Lambda}_1 \mathbf{n} = -\nabla \Theta_2 \cdot \mathbf{\Lambda}_2 \mathbf{n}, \tag{26}$$

$$-\left[\mathbf{I} \otimes \mathbf{n}^T \right] \mathbf{S}_1 (\nabla \otimes \mathbf{u}_1) + p_{\beta 1} \mathbf{B}_1 \mathbf{n} + \Theta_{\beta 1} \mathbf{A}_1 \mathbf{n} = -\left[\mathbf{I} \otimes \mathbf{n}^T \right] \mathbf{S}_2 (\nabla \otimes \mathbf{u}_2) + p_{\beta 2} \mathbf{B}_2 \mathbf{n} + \Theta_{\beta 2} \mathbf{A}_2 \mathbf{n}, \tag{27}$$

where $\mathbf{d}_1$ and $\mathbf{d}_2$ are unknowns at the cell centers, $\mathbf{x}_1$ and $\mathbf{x}_2$ are the positions of the cell centers, $\otimes$ denotes the Kronecker product, $\mathbf{x}_\beta$ denotes the center of the interface, subscripts $\beta 1$ and $\beta 2$ denote the single-side interpolations of respective properties to the interface β, $\mathbf{I} \otimes (\mathbf{x}_\beta - \mathbf{x}_1)^T$ and $\mathbf{I} \otimes (\mathbf{x}_\beta - \mathbf{x}_2)^T$ represent 5×15 matrices constructed as

$$\mathbf{I} \otimes (\mathbf{x}_\beta - \mathbf{x}_i)^T = \begin{pmatrix} (\mathbf{x}_\beta - \mathbf{x}_i)^T & & & & \\ & (\mathbf{x}_\beta - \mathbf{x}_i)^T & & & \\ & & (\mathbf{x}_\beta - \mathbf{x}_i)^T & & \\ & & & (\mathbf{x}_\beta - \mathbf{x}_i)^T & \\ & & & & (\mathbf{x}_\beta - \mathbf{x}_i)^T \end{pmatrix}, \quad i = 1, 2,$$

$\mathbf{I} \otimes \mathbf{n}^T$ stands for 3×9 matrix constructed in a similar way, $\nabla \otimes \mathbf{d}_1$, $\nabla \otimes \mathbf{d}_2$ and $\nabla \otimes \mathbf{u}_1$, $\nabla \otimes \mathbf{u}_2$ are 15×1 and 9×1 vectors respectively, constructed as

$$\nabla \otimes \mathbf{d}_i = \begin{pmatrix} \nabla p \\ \nabla \Theta \\ \nabla \otimes \mathbf{u} \end{pmatrix}_i = \begin{pmatrix} \nabla p \\ \nabla \Theta \\ \nabla u_x \\ \nabla u_y \\ \nabla u_z \end{pmatrix}_i, \quad i = 1, 2, \tag{28}$$

where $\begin{bmatrix} u_x u_y u_z \end{bmatrix}^T$ are the components of displacement vector $\mathbf{u}$. Note that the arguments are swapped in the definitions of vectors $\nabla \otimes \mathbf{d}$ and $\nabla \otimes \mathbf{u}$ in Eq. (28). Additionally, $\mathbf{S}_1 = \mathbf{\Gamma} \mathbf{C}_1 \mathbf{\Gamma}^T$, $\mathbf{S}_2 = \mathbf{\Gamma} \mathbf{C}_2 \mathbf{\Gamma}^T$ are 9×9 matrices where $\mathbf{C}$ denotes a 6×6 symmetric stiffness matrix in Voigt notation and where

$$\mathbf{\Gamma}^T = \begin{bmatrix} 1 & 0 & 0 & 0 & 0 & 0 & 0 & 0 & 0 \\ 0 & 0 & 0 & 0 & 1 & 0 & 0 & 0 & 0 \\ 0 & 0 & 0 & 0 & 0 & 0 & 0 & 0 & 1 \\ 0 & 0 & 0 & 0 & 0 & 1 & 0 & 1 & 0 \\ 0 & 0 & 1 & 0 & 0 & 0 & 1 & 0 & 0 \\ 0 & 1 & 0 & 1 & 0 & 0 & 0 & 0 & 0 \end{bmatrix}.$$

Flux balances in Eqs. (25), (26), and (27) stem from Darcy's, Fourier's and momentum fluxes, i.e. traction vectors, in Eqs. (19). While the momentum flux balance accounts for all contributions to total momentum flux, the local balance of fluid mass flux in Eq. (25) neglects the fluxes caused by matrix movement and molecular diffusion. Additionally, the local balance of energy in Eq. (26) neglects heat convection fluxes. Nonetheless, the conservation of Darcy's fluxes in Eq. (25) and the use of SPU approximation for mobility multipliers can guarantee the sufficiency of Eq. (26) for the conservation of cumulative heat convection and conduction fluxes.

Eqs. (24)–(27) reveal that the local problem decomposes into three subproblems: fluid mass, heat and momentum. The fluid mass and heat subproblems are completely independent while the momentum subproblem depends on both of them. Therefore, we first remind the approximations for the fluid mass and heat subproblems.

Fluid mass and heat conduction fluxes. For the derivation of MPFA for Darcy's and Fourier's fluxes, pressure and temperature interpolations we follow approach described in Terekhov et al. [56]. We employ the co-normal decompositions of gradients and properties

$$\nabla p_i = \xi_i^p \mathbf{n} + \boldsymbol{\xi}_{\tau i}^p, \qquad \xi_i^p = \mathbf{n}^T \nabla p_i, \qquad \boldsymbol{\xi}_{\tau i}^p = (\mathbf{I} - \mathbf{n} \mathbf{n}^T) \nabla p_i, \tag{29}$$

$$\nabla \Theta_i = \xi_i^\theta \mathbf{n} + \boldsymbol{\xi}_{\tau i}^\theta, \qquad \xi_i^\theta = \mathbf{n}^T \nabla \Theta_i, \qquad \boldsymbol{\xi}_{\tau i}^\theta = (\mathbf{I} - \mathbf{n} \mathbf{n}^T) \nabla \Theta_i, \tag{30}$$

$$\mathbf{K}_i \mathbf{n} = \kappa_i \mathbf{n} + \boldsymbol{\kappa}_i, \qquad \kappa_i = \mathbf{n}^T \mathbf{K}_i \mathbf{n}, \qquad \boldsymbol{\kappa}_i = (\mathbf{I} - \mathbf{n} \mathbf{n}^T) \mathbf{K}_i \mathbf{n}, \tag{31}$$

$$\mathbf{\Lambda}_i \mathbf{n} = \lambda_i \mathbf{n} + \boldsymbol{\lambda}_i, \qquad \lambda_i = \mathbf{n}^T \mathbf{\Lambda}_i \mathbf{n}, \qquad \boldsymbol{\lambda}_i = (\mathbf{I} - \mathbf{n} \mathbf{n}^T) \mathbf{\Lambda}_i \mathbf{n}, \tag{32}$$

where ξ_i^p, ξ_i^θ and $\boldsymbol{\xi}_{\tau i}^p$, $\boldsymbol{\xi}_{\tau i}^\theta$ are normal and tangential projections, respectively, of pressure and temperature gradients evaluated in cells $i = 1, 2$. Note that $\boldsymbol{\xi}_{\tau 1}^p = \boldsymbol{\xi}_{\tau 2}^p = \boldsymbol{\xi}_\tau^p$ and $\boldsymbol{\xi}_{\tau 1}^\theta = \boldsymbol{\xi}_{\tau 2}^\theta = \boldsymbol{\xi}_\tau^\theta$ due to Eq. (24). Moreover, scalars κ_i, λ_i and vectors $\boldsymbol{\kappa}_i, \boldsymbol{\lambda}_i$ represent normal and tangential projections, respectively, of $\mathbf{K}_i \mathbf{n}$ and $\mathbf{\Lambda}_i \mathbf{n}$ for cells $i = 1, 2$.
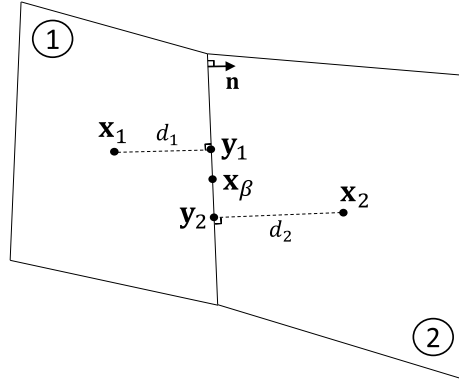
Fig. 1. Normal decomposition of distances between the centers $\mathbf{x}_i$ of cells $i = 1, 2$ and the center $\mathbf{x}_\beta$ of interface β.

By substituting Eqs. (25) and (26) into Eq. (24), the gradients ξ_2^p and ξ_2^θ can be eliminated, yielding the following equations for pressure gradient $\nabla \mathrm{p}_1$ and temperature gradient $\nabla \Theta_1$

$$\left(\kappa_2(\mathbf{x}_2 - \mathbf{x}_1) + \mathrm{d}_2(\mathbf{K}_1 - \mathbf{K}_2)\mathbf{n}\right)^T \nabla \mathrm{p}_1 = \kappa_2(\mathrm{p}_2 - \mathrm{p}_1) + \mathrm{d}_2 \rho_\mathrm{f} \mathrm{g} \nabla D^T \left(\mathbf{K}_2 - \mathbf{K}_1\right)\mathbf{n}, \tag{33}$$

$$\left(\lambda_2(\mathbf{x}_2 - \mathbf{x}_1) + \mathrm{d}_2(\mathbf{\Lambda}_1 - \mathbf{\Lambda}_2)\mathbf{n}\right)^T \nabla \Theta_1 = \lambda_2(\Theta_2 - \Theta_1), \tag{34}$$

which we use below for the reconstruction of cell-centered gradients in cell 1.

In a similar fashion the gradients ξ_2^p and ξ_2^θ can be eliminated in the Eqs. (25) and (26), yielding MPFA of Darcy's and Fourier's fluxes

$$\mathrm{q}_\beta^\mathrm{f} = \kappa(\mathrm{p}_1 - \mathrm{p}_2) - \left(\kappa(\mathbf{y}_1 - \mathbf{y}_2)^T + \frac{\mathrm{d}_1\kappa_2\boldsymbol{\kappa}_1^T + \mathrm{d}_2\kappa_1\boldsymbol{\kappa}_2^T}{\mathrm{d}_2\kappa_1 + \mathrm{d}_1\kappa_2}\right)\boldsymbol{\xi}_\tau^p y + \rho_\mathrm{f}\mathrm{g}\nabla D \cdot \frac{\mathrm{d}_1\kappa_2\mathbf{K}_1 + \mathrm{d}_2\kappa_1\mathbf{K}_2}{\mathrm{d}_2\kappa_1 + \mathrm{d}_1\kappa_2}\mathbf{n} \tag{35}$$

$$\mathrm{q}_\beta^\theta = \lambda(\Theta_1 - \Theta_2) - \left(\lambda(\mathbf{y}_1 - \mathbf{y}_2)^T + \frac{\mathrm{d}_1\lambda_2\boldsymbol{\lambda}_1^T + \mathrm{d}_2\lambda_1\boldsymbol{\lambda}_2^T}{\mathrm{d}_2\lambda_1 + \mathrm{d}_1\lambda_2}\right)\boldsymbol{\xi}_\tau^\theta, \tag{36}$$

where $\kappa = \kappa_1\kappa_2(\mathrm{d}_1\kappa_2 + \mathrm{d}_2\kappa_1)^{-1}$, $\lambda = \lambda_1\lambda_2(\mathrm{d}_1\lambda_2 + \mathrm{d}_2\lambda_1)^{-1}$ are weighted harmonic mean permeability and heat conductivity, respectively. Additionally, the following decompositions of geometrical terms are utilized

$$\mathbf{x}_\beta - \mathbf{x}_1 = \mathrm{d}_1\mathbf{n} + (\mathbf{x}_\beta - \mathbf{y}_1), \qquad \mathrm{d}_1 = \mathbf{n} \cdot (\mathbf{x}_\beta - \mathbf{x}_1) > 0, \qquad \mathbf{y}_1 = \mathbf{x}_1 + \mathrm{d}_1\mathbf{n},$$

$$\mathbf{x}_2 - \mathbf{x}_\beta = \mathrm{d}_2\mathbf{n} + (\mathbf{y}_2 - \mathbf{x}_\beta), \qquad \mathrm{d}_2 = \mathbf{n} \cdot (\mathbf{x}_2 - \mathbf{x}_\beta) > 0, \qquad \mathbf{y}_2 = \mathbf{x}_2 - \mathrm{d}_2\mathbf{n}, \tag{37}$$

where d_i denotes a distance from the cell center $\mathbf{x}_i$, $i = 1, 2$ to an interface β while $\mathbf{y}_i$ stands for a normal projection of cell center $\mathbf{x}_i$, $i = 1, 2$ onto interface β. These geometrical terms are shown in Fig. 1.

Finally, by substituting the gradients ξ_1^p and ξ_1^θ into the left-hand side of Eq. (24) one can obtain the pressure and temperature interpolations at the center of the interface β

$$\mathrm{p}_\beta = (\mathrm{d}_1\kappa_2 + \mathrm{d}_2\kappa_1)^{-1}(\mathrm{d}_2\kappa_1\mathrm{p}_1 + \mathrm{d}_1\kappa_2\mathrm{p}_2) + (\mathrm{d}_1\kappa_2 + \mathrm{d}_2\kappa_1)^{-1}\left(\left(\mathrm{d}_1\mathrm{d}_2(\boldsymbol{\kappa}_2 - \boldsymbol{\kappa}_1)^T + \mathrm{d}_2\kappa_1(\mathbf{x}_\beta - \mathbf{y}_1)^T + \mathrm{d}_1\kappa_2(\mathbf{x}_\beta - \mathbf{y}_2)^T\right)\boldsymbol{\xi}_\tau^p + \right.$$
$$\left. + \mathrm{d}_1\mathrm{d}_2\rho_\mathrm{f}\mathrm{g}\nabla D^T(\mathbf{K}_1 - \mathbf{K}_2)\mathbf{n}\right), \tag{38}$$

$$\Theta_\beta = (\mathrm{d}_1\lambda_2 + \mathrm{d}_2\lambda_1)^{-1}(\mathrm{d}_2\lambda_1\Theta_1 + \mathrm{d}_1\lambda_2\Theta_2) + (\mathrm{d}_1\lambda_2 + \mathrm{d}_2\lambda_1)^{-1}\left(\mathrm{d}_1\mathrm{d}_2(\boldsymbol{\lambda}_2 - \boldsymbol{\lambda}_1)^T + \mathrm{d}_2\lambda_1(\mathbf{x}_\beta - \mathbf{y}_1)^T + \mathrm{d}_1\lambda_2(\mathbf{x}_\beta - \mathbf{y}_2)^T\right)\boldsymbol{\xi}_\tau^\theta. \tag{39}$$

Momentum fluxes. The same approach is utilized for the multi-point approximation of momentum fluxes, i.e. traction vectors, and for the interpolation of displacements. Following the similar procedure [16], we consider the co-normal decompositions of displacement gradients and stiffnesses as

$$\nabla \otimes \mathbf{u}_i = [\mathbf{I} \otimes \mathbf{n}]\boldsymbol{\xi}_i^u + \boldsymbol{\xi}_{\tau i}^u, \quad \boldsymbol{\xi}_i^u = [\mathbf{I} \otimes \mathbf{n}^T]\left[\nabla \otimes \mathbf{u}_i\right], \quad \boldsymbol{\xi}_{\tau i}^u = [\mathbf{I} \otimes (\mathbf{I} - \mathbf{n}\mathbf{n}^T)]\left[\nabla \otimes \mathbf{u}_i\right], \tag{40}$$

$$\left[\mathbf{I} \otimes \mathbf{n}^T\right]\mathbf{S}_i = \mathbf{T}_i[\mathbf{I} \otimes \mathbf{n}^T] + \boldsymbol{\Gamma}_i, \quad \mathbf{T}_i = [\mathbf{I} \otimes \mathbf{n}^T]\mathbf{S}_i[\mathbf{I} \otimes \mathbf{n}], \quad \boldsymbol{\Gamma}_i = [\mathbf{I} \otimes \mathbf{n}^T]\mathbf{S}_i[\mathbf{I} \otimes (\mathbf{I} - \mathbf{n}\mathbf{n}^T)], \tag{41}$$

where $\boldsymbol{\xi}_i^u$ and $\boldsymbol{\xi}_{\tau i}^u$ are the normal and tangential projections of displacement gradients, respectively, evaluated in cells $i = 1, 2$, $\mathbf{T}_i$ and $\boldsymbol{\Gamma}_i$ are normal and tangential projections of $\left[\mathbf{I} \otimes \mathbf{n}^T\right]\mathbf{S}_i$, respectively, evaluated in cells $i = 1, 2$. Note that $\boldsymbol{\xi}_{\tau 1}^u = \boldsymbol{\xi}_{\tau 2}^u = \boldsymbol{\xi}_\tau^u$ due to Eq. (24).

By substituting Eq. (27) into Eq. (24), the gradient $\boldsymbol{\xi}_2^u$ can be eliminated, yielding the following equations for displacement gradient $\nabla \otimes \mathbf{u}_1$

$$\left(\mathbf{T}_2 \otimes (\mathbf{x}_2 - \mathbf{x}_1)^T + \mathrm{d}_2(\mathbf{T}_1 - \mathbf{T}_2) \otimes \mathbf{n}^T + \mathrm{d}_2(\boldsymbol{\Gamma}_1 - \boldsymbol{\Gamma}_2)\right)[\nabla \otimes \mathbf{u}_1] = \mathbf{T}_2(\mathbf{u}_2 - \mathbf{u}_1) + \mathrm{d}_2\left(\mathrm{p}_{\beta 1}\mathbf{B}_1 + \Theta_{\beta 1}\mathbf{A}_1 - \mathrm{p}_{\beta 2}\mathbf{B}_2 - \Theta_{\beta 2}\mathbf{A}_2\right)\mathbf{n}, \tag{42}$$

where the approximations for $p_{\beta 1}$, $\Theta_{\beta 1}$ are defined in Eq. (24) while the following approximations of $p_{\beta 2}$ and $\Theta_{\beta 2}$, which depend on the pressure and temperature gradients, respectively, evaluated in cell 1, are used

$$p_{\beta 2} = p_2 + (\mathbf{x}_\beta - \mathbf{y}_2 - d_2 \kappa_2^{-1}(\mathbf{K}_1 \mathbf{n} - \boldsymbol{\kappa}_2))^T \nabla p_1 + d_2 \kappa_2^{-1} \rho_f g \nabla D^T (\mathbf{K}_1 - \mathbf{K}_2) \mathbf{n}, \tag{43}$$

$$\Theta_{\beta 2} = \Theta_2 + (\mathbf{x}_\beta - \mathbf{y}_2 - d_2 \lambda_2^{-1}(\boldsymbol{\Lambda}_1 \mathbf{n} - \boldsymbol{\lambda}_2))^T \nabla \Theta_1. \tag{44}$$

By deriving $\boldsymbol{\xi}_1^u$ from Eqs. (24) and (27) and substituting it to the left-hand side of Eq. (27), we can assemble the approximation of the total traction at the interface β as

$$\mathbf{f}_\beta = \mathbf{f}_\beta^d + \mathbf{f}_\beta^a, \tag{45}$$

where

$$\mathbf{f}_\beta^d = -\mathbf{T}_1 \boldsymbol{\xi}_1^u - \boldsymbol{\Gamma}_1 \boldsymbol{\xi}_\tau^u = \mathbf{T}(\mathbf{u}_1 - \mathbf{u}_2) - \left([\mathbf{T} \otimes (\mathbf{y}_1 - \mathbf{y}_2)^T] + d_1 \mathbf{T}_2 (d_1 \mathbf{T}_2 + d_2 \mathbf{T}_1)^{-1} \boldsymbol{\Gamma}_1 + d_2 \mathbf{T}_1 (d_1 \mathbf{T}_2 + d_2 \mathbf{T}_1)^{-1} \boldsymbol{\Gamma}_2\right) \boldsymbol{\xi}_\tau^u$$
$$+ d_2 \mathbf{T}_1 (d_1 \mathbf{T}_2 + d_2 \mathbf{T}_1)^{-1} (p_\beta(\mathbf{B}_2 - \mathbf{B}_1) + \Theta_\beta(\mathbf{A}_2 - \mathbf{A}_1)) \mathbf{n}, \tag{46}$$

$$\mathbf{f}_\beta^a = (p_\beta \mathbf{B}_1 + \Theta_\beta \mathbf{A}_1) \mathbf{n}, \tag{47}$$

and $\mathbf{T} = \mathbf{T}_1 (d_1 \mathbf{T}_2 + d_2 \mathbf{T}_1)^{-1} \mathbf{T}_2$ stands for 3×3 matrix and the approximations for p_β, Θ_β are taken from Eqs. (38) and (39). The equation for the assembled total traction will look like

$$\mathbf{f}_\beta = \mathbf{T}(\mathbf{u}_1 - \mathbf{u}_2) - \left([\mathbf{T} \otimes (\mathbf{y}_1 - \mathbf{y}_2)^T] + d_1 \mathbf{T}_2 (d_1 \mathbf{T}_2 + d_2 \mathbf{T}_1)^{-1} \boldsymbol{\Gamma}_1 + d_2 \mathbf{T}_1 (d_1 \mathbf{T}_2 + d_2 \mathbf{T}_1)^{-1} \boldsymbol{\Gamma}_2\right) \boldsymbol{\xi}_\tau^u \tag{48}$$
$$+ d_1 \mathbf{T}_2 (d_1 \mathbf{T}_2 + d_2 \mathbf{T}_1)^{-1} (p_\beta \mathbf{B}_1 + \Theta_\beta \mathbf{A}_1) \mathbf{n} + d_2 \mathbf{T}_1 (d_1 \mathbf{T}_2 + d_2 \mathbf{T}_1)^{-1} (p_\beta \mathbf{B}_2 + \Theta_\beta \mathbf{A}_2) \mathbf{n},$$

which is symmetric against simultaneous swap of indices $1 \leftrightarrow 2$ and normal direction $\mathbf{n} \leftrightarrow -\mathbf{n}$.

The advective term $\tilde{q}_\beta = (\mathbf{u}_2 - \mathbf{u}_1) \cdot \mathbf{B}_1 \mathbf{n}$ depends on the approximation of displacements at the center of an interface $\mathbf{u}_\beta$. This approximation can be obtained in a similar fashion, by deriving $\boldsymbol{\xi}_1^u$ from Eqs. (24) and (27), but substituting it to the left-hand side of Eq. (24). The resulting expression reads as

$$\mathbf{u}_\beta = (d_1 \mathbf{T}_2 + d_2 \mathbf{T}_1)^{-1}(d_2 \mathbf{T}_1 \mathbf{u}_1 + d_1 \mathbf{T}_2 \mathbf{u}_2) + (d_1 \mathbf{T}_2 + d_2 \mathbf{T}_1)^{-1}\left((d_1 d_2(\boldsymbol{\Gamma}_2 - \boldsymbol{\Gamma}_1) + d_2 \mathbf{T}_1 \otimes (\mathbf{x}_\beta - \mathbf{y}_1)^T + d_1 \mathbf{T}_2 \otimes (\mathbf{x}_\beta - \mathbf{y}_2)^T\right)\boldsymbol{\xi}_\tau^u +$$
$$+ d_1 d_2(p_{\beta 1} \mathbf{B}_1 + \Theta_{\beta 1} \mathbf{A}_1 - p_{\beta 2} \mathbf{B}_2 - \Theta_{\beta 2} \mathbf{A}_2) \mathbf{n}, \tag{49}$$

where single-side pressure $p_{\beta 1}, p_{\beta 2}$ and temperature $\Theta_{\beta 1}, \Theta_{\beta 2}$ interpolations are taken from Eq. (24).

The approximation of traction vector at the interior interfaces is provided in Eqs. (45)–(47). Additionally, the interpolation of displacements required for the evaluation of porosity in Eqs. (22) and (23) is provided in Eq. (49). The novelty of these approximations is that they account for thermal stresses and, therefore, incorporate temperature. Note that all these approximations are yet incomplete and require the substitution of suitable approximation of gradients explained below.

2.3.2. Approximation of fluxes at boundary interfaces

The approximations of fluxes at boundary interfaces must satisfy corresponding boundary conditions defined in Eqs. (14)–(17). They replace the local problem, which we use for interior interfaces, and allow meaningful flux approximations to be derived at the domain's boundaries. We employ the single-side approximations from the left-hand side of Eqs. (24)–(27). In particular, using the single-side approximation of normal pressure gradient ξ_1^p one can derive pressure p_b and Darcy's flux $q_{\alpha,b}^f$ at the boundary interface as [16]

$$p_b = \left(\alpha_p + \frac{\beta_p \kappa_1}{d_1}\right)^{-1}\left(\gamma_p + \frac{\beta_p \kappa_1}{d_1} p_1 - \beta_p\left(\frac{\kappa_1}{d_1}(\mathbf{y}_1 - \mathbf{x}_b) + \boldsymbol{\kappa}_1\right) \cdot \boldsymbol{\xi}_\tau^p + \beta_p \rho_f g \nabla D \cdot \mathbf{K}_1 \mathbf{n}\right), \tag{50}$$

$$q_{\alpha,b}^f = -\left(\alpha_p + \frac{\beta_p \kappa_1}{d_1}\right)^{-1} \tag{51}$$
$$\left(\frac{\kappa_1}{d_1}\gamma_p - \alpha_p \frac{\kappa_1}{d_1} p_1 + \alpha_p\left(\frac{\kappa_1}{d_1}(\mathbf{y}_1 - \mathbf{x}_b) + \boldsymbol{\kappa}_1\right) \cdot \boldsymbol{\xi}_\tau^p - \alpha_p \rho_\alpha g \nabla D \cdot \mathbf{K}_1 \mathbf{n}\right),$$

where $\mathbf{x}_b$ denotes the center of boundary interface, $\alpha_p, \beta_p, \gamma_p$ are the coefficients defining boundary conditions in Eq. (14). The same technique can be applied to derive the temperature Θ_b and Fourier's flux q_b^θ at the boundary interface as

$$\Theta_b = \left(\alpha_\theta + \frac{\beta_\theta \lambda_1}{d_1}\right)^{-1}\left(\gamma_\theta + \frac{\beta_\theta \lambda_1}{d_1}\Theta_1 - \beta_\theta\left(\frac{\lambda_1}{d_1}(\mathbf{y}_1 - \mathbf{x}_b) + \boldsymbol{\lambda}_1\right) \cdot \boldsymbol{\xi}_\tau^\theta\right), \tag{52}$$

$$q_b^\theta = -\left(\alpha_\theta + \frac{\beta_\theta \lambda_1}{d_1}\right)^{-1}\left(\frac{\lambda_1}{d_1}\gamma_\theta - \alpha_\theta \frac{\lambda_1}{d_1}\Theta_1 + \alpha_\theta\left(\frac{\lambda_1}{d_1}(\mathbf{y}_1 - \mathbf{x}_b) + \boldsymbol{\lambda}_1\right) \cdot \boldsymbol{\xi}_\tau^\theta\right), \tag{53}$$

where $\alpha_\theta, \beta_\theta, \gamma_\theta$ are the coefficients defining boundary conditions in Eq. (15). Similarly, one can substitute the single-side approximation of displacement gradients $\boldsymbol{\xi}_1^u$ to boundary conditions in Eqs. (16) and (17) to derive $\mathbf{u}_b$ and the total traction vector at the boundary interface as

$$\mathbf{u}_b = \left(\alpha_t \mathbf{I} + \frac{\beta_t}{d_1}\mathbf{T}_1\right)^{-1}\left(l\gamma_n\mathbf{n} + (\mathbf{I} - l\mathbf{nn}^T\mathbf{L})\boldsymbol{\gamma}_t\right)+$$

$$+ \left(\alpha_t \mathbf{I} + \frac{\beta_t}{d_1}\mathbf{T}_1\right)^{-1}\left(\beta_t \mathbf{I} + l\mathbf{nn}^T(\beta_n\mathbf{I} - \beta_t\mathbf{L})\right)\cdot$$

$$\cdot\left(\frac{1}{d_1}\mathbf{T}_1\mathbf{u}_1 - \left(\frac{1}{d_1}\mathbf{T}_1\left[\mathbf{I} \otimes (\mathbf{y}_1 - \mathbf{x}_b)^T\right] + \boldsymbol{\Gamma}_1\right)\boldsymbol{\xi}_\tau^u + p_b\mathbf{B}_1\mathbf{n} + \Theta_b\mathbf{A}_1\mathbf{n}\right), \tag{54}$$

$$\mathbf{f}_b = -\frac{1}{d_1}\mathbf{T}_1\left(\alpha_t\mathbf{I} + \frac{\beta_t}{d_1}\mathbf{T}_1\right)^{-1}\left(l\gamma_n\mathbf{n} + (\mathbf{I} - l\mathbf{nn}^T\mathbf{L})\boldsymbol{\gamma}_t\right)$$

$$- \frac{1}{d_1}\mathbf{T}_1\left(\alpha_t\mathbf{I} + \frac{\beta_t}{d_1}\mathbf{T}_1\right)^{-1}\left(l\mathbf{nn}^T(\beta_n\mathbf{I} - \beta_t\mathbf{L}) - \alpha_t d_1\mathbf{T}_1^{-1}\right)\cdot$$

$$\cdot\left(\frac{1}{d_1}\mathbf{T}_1\mathbf{u}_1 - \left(\frac{1}{d_1}\mathbf{T}_1\left[\mathbf{I} \otimes (\mathbf{y}_1 - \mathbf{x}_b)\right] + \boldsymbol{\Gamma}_1\right)\boldsymbol{\xi}_\tau^u + p_b\mathbf{B}_1\mathbf{n} + \Theta_b\mathbf{A}_1\mathbf{n}\right), \tag{55}$$

where $\mathbf{L} = \left(\alpha_n\mathbf{I} + \frac{\beta_n}{d_1}\mathbf{T}_1\right)\left(\alpha_t\mathbf{I} + \frac{\beta_t}{d_1}\mathbf{T}_1\right)^{-1}$ is a 3×3 matrix, $l = (\mathbf{n}^T\mathbf{L}\mathbf{n})^{-1}$ is a scalar and the approximations of p_b and Θ_b are defined in Eqs. (50) and (52), respectively, $\alpha_n, \beta_n, \gamma_n$ and $\alpha_t, \beta_t, \boldsymbol{\gamma}_t$ are the coefficients defining normal Eq. (16) and tangential Eq. (17) boundary conditions. The approximation of $\tilde{q}_\beta$ in Eq. (23) can be achieved from Eq. (54).

Eqs. (50), (52), and (54) can be rewritten for the reconstruction of gradients in the cells with boundary interfaces as

$$(\alpha_p(\mathbf{x}_b - \mathbf{x}_1) + \beta_p\mathbf{K}_1\mathbf{n})\cdot\nabla p_1 = \gamma_p + \beta_p\rho_f g\nabla D \cdot \mathbf{K}_1\mathbf{n} - \alpha_p p_1, \tag{56}$$

$$(\alpha_\theta(\mathbf{x}_b - \mathbf{x}_1) + \beta_\theta\boldsymbol{\Lambda}_1\mathbf{n})\cdot\nabla\Theta_1 = \gamma_\theta - \alpha_\theta\Theta_1, \tag{57}$$

$$\left(\alpha_t\left[\mathbf{I} \otimes (\mathbf{x}_b - \mathbf{x}_1)^T\right] + \beta_t\left[\mathbf{I} \otimes \mathbf{n}^T\right]\mathbf{S}_1 +\right.$$

$$+ \left.l\mathbf{nn}^T(\beta_n\mathbf{I} - \beta_t\mathbf{L})\left(\boldsymbol{\Gamma}_1 + \frac{1}{d_1}\mathbf{T}_1\left[\mathbf{I} \otimes (\mathbf{y}_1 - \mathbf{x}_b)^T\right]\right)\right)\left[\nabla \otimes \mathbf{u}_1\right] =$$

$$= l\gamma_n\mathbf{n} + (\mathbf{I} - l\mathbf{nn}^T\mathbf{L})\boldsymbol{\gamma}_t + \left(l\mathbf{nn}^T(\beta_n\mathbf{I} - \beta_t\mathbf{L})\frac{1}{d_1}\mathbf{T}_1 - \alpha_t\mathbf{I}\right)\mathbf{u}_1 +$$

$$+ (\beta_t\mathbf{I} + l\mathbf{nn}^T(\beta_n\mathbf{I} - \beta_t\mathbf{L}))(p_b\mathbf{B}_1 + \Theta_b\mathbf{A}_1)\mathbf{n}, \tag{58}$$

where the approximations of p_b and Θ_b, required for the latter equation, are provided in Eqs. (50) and (52), respectively.

2.3.3. Reconstruction of gradients

The reconstruction of pressure and temperature gradients can be performed independently. Bringing together Eqs. (33) and (34) for interior interfaces and, whenever suitable, Eqs. (56) and (57) for boundary interfaces of a cell, we build up the independent systems with respect to pressure and temperature gradients. Considering N interfaces of the j-th cell, we achieve the following systems

$$\mathbf{M}_j^p\nabla p_j = \mathbf{D}_j^p\boldsymbol{\psi}_j^p, \quad \mathbf{M}_j^\theta\nabla\Theta_j = \mathbf{D}_j^\theta\boldsymbol{\psi}_j^\theta, \tag{59}$$

where $\mathbf{M}_j^p$ and $\mathbf{M}_j^\theta$ are $N \times 3$ matrices of coefficients in front of the pressure and temperature gradients, respectively, at the left-hand side of the equations and $\mathbf{D}_j^p$ and $\mathbf{D}_j^\theta$ are $N \times (N + 1)$ matrices of coefficients in front of the unknowns and free terms in boundary conditions at the right-hand side of the temperature and pressure equations, respectively, while $\boldsymbol{\psi}_j^p$ and $\boldsymbol{\psi}_j^\theta$ are $(N + 1) \times 1$ vectors of $N + 1$ unknown pressures p_i or free terms γ_p in mass boundary conditions and temperatures Θ_i or free terms γ_θ in thermal boundary conditions, respectively. The solution of Eqs. (59) can be obtained in a least-squares sense as

$$\nabla p_j = (\mathbf{M}_j^{pT}\mathbf{M}_j^p)^{-1}\mathbf{M}_j^{pT}\mathbf{D}_j^p\boldsymbol{\psi}_j^p, \quad \nabla\Theta_j = (\mathbf{M}_j^{\theta T}\mathbf{M}_j^\theta)^{-1}\mathbf{M}_j^{\theta T}\mathbf{D}_j^\theta\boldsymbol{\psi}_j^\theta. \tag{60}$$

The reconstruction of displacement gradients depends on pressure and temperature gradients. Thus, we evaluate pressure and temperature gradients in all cells first and, subsequently, substitute them into the reconstruction of displacement gradients. We utilize the same approach for the reconstruction of displacement gradients. We assemble Eq. (42) for interior and Eq. (58) for boundary interfaces, forming the system of N equations

$$\mathbf{M}_j^u(\nabla \otimes \mathbf{u}_j) = \mathbf{D}_j^u\boldsymbol{\psi}_j^u, \tag{61}$$

independently for every j-th cell, where $\mathbf{M}_j^u$ is a $3N \times 9$ matrix of coefficients in front of the displacement gradients at the left-hand side of the equations, and $\mathbf{D}_j^u$ is $3N \times 5(N + 1)$ matrix of coefficients in front of the corresponding unknowns and free terms in boundary conditions at the right-hand side the equations, while $\boldsymbol{\psi}_j^u$ is $5(N + 1) \times 1$ vectors of $5(N + 1)$ unknown $\mathbf{d}_i$ or free terms $\gamma_p, \gamma_\theta, \gamma_n, \boldsymbol{\gamma}_t$ in boundary conditions. The least-squares solution of the system in Eq. (61) is

$$\nabla \otimes \mathbf{u}_j = (\mathbf{M}_j^{uT}\mathbf{M}_j^u)^{-1}\mathbf{M}_j^{uT}\mathbf{D}_j^u\boldsymbol{\psi}_j^u. \tag{62}$$

The flux approximations and interpolations depend on the tangential projections $\boldsymbol{\xi}_\tau = \{\boldsymbol{\xi}_\tau^p, \boldsymbol{\xi}_\tau^\theta, \boldsymbol{\xi}_\tau^u\}$ of pressure, temperature and displacement gradients, respectively, evaluated at the interface. For boundary interfaces, we employ a single-side approximation of
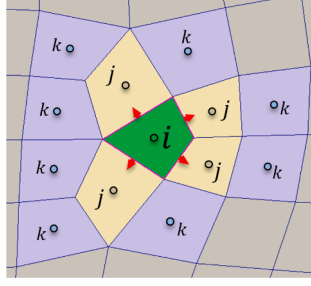
Fig. 2. Cells that contribute to the approximation of fluxes over the interfaces of cell i. Index j denotes the nearest neighbors of cell i. Index k denotes farther neighbors that contribute to the gradients reconstructed in cells j.

those gradients, i.e. $\boldsymbol{\xi}_\tau = \boldsymbol{\xi}_{1\tau}$. For interior interfaces, we utilize the arithmetic mean

$$\boldsymbol{\xi}_\tau = \frac{\boldsymbol{\xi}_{\tau 1} + \boldsymbol{\xi}_{\tau 2}}{2}. \tag{63}$$

A set of cells that contribute to the approximation Eq. (63) for each interface of some cell j is illustrated in Fig. 2.

It is worth mentioning that the least squares solution in Eq. (60) allows computing the gradients of unknowns locally and independently for every cell. Note, however, that it does not strictly guarantee the local conservation property for the scheme as least-squares solution of the system, assembled for all cell's interfaces, can violate individual equations. In order to maintain the local conservation, individual gradients for every interface that respects the corresponding flux balance should be employed [56,57].

2.4. Discretization in state space

The simulation of multiphase compositional thermal fluid flow requires efficient machinery for the evaluation of fluid properties and their derivatives. Although corresponding constitutive and equilibrium relations usually remain fixed across domain, this evaluation often consumes significant development and computational resources. In this paper, we employ the Operator-based Linearization (OBL) which is designed to overcome this challenge by simplifying the treatment of state-dependent operators, providing efficient and flexible means for Jacobian and residual assembly [59].

OBL implies the calculation of the operators dependent on a single-cell state $\boldsymbol{\omega} = \{p, \mathbf{z}_i, \Theta\}$, i.e.

$$\{\mathfrak{a}_i, \mathfrak{a}_e, x_{i\alpha}\rho_\alpha k_{r\alpha}\mu_\alpha^{-1}, \rho_\alpha, h_\alpha, S_\alpha, \rho_s, \mathfrak{r}_i, \mathfrak{r}_e\} = \mathbf{f}(\widetilde{\boldsymbol{\omega}}), \tag{64}$$

at predefined grid nodes $\widetilde{\boldsymbol{\omega}}$ covering the state space. For regular grid we have

$$\widetilde{\boldsymbol{\omega}} = \widetilde{p} \times \widetilde{z}_1 \times \cdots \times \widetilde{z}_{n_c} \times \widetilde{\Theta}, \tag{65}$$

$$\widetilde{p} = \{p_1, \ldots, p_{N_p}\}, \quad \widetilde{z}_1 = \{z_{1,1}, \ldots, z_{1,N_{z1}}\}, \ldots, \widetilde{z}_{n_c} = \{z_{n_c,1}, \ldots, z_{n_c,N_{zn_c}}\}, \tag{66}$$

$$\widetilde{\Theta} = \{\Theta_1, \ldots, \Theta_{N_T}\},$$

where $\widetilde{p}, \widetilde{z}_i$ and $\widetilde{\Theta}$ denote state-space axes coordinates, $\mathbf{f}$ is multilinear interpolant function used to reconstruct operator values between supporting points. Regular grid guarantees fast evaluation of derivatives. The distribution of points along axes in Eq. (66) can be dictated by specific model properties, e.g. for better resolution of phase envelope. By default, they are distributed uniformly for simplicity.

We utilize the adaptive operator sampling strategy for the evaluation of operators defined in Eq. (64). For any requested state, the method identifies the set of supporting points required for interpolation. If any of these points have not yet been evaluated, the exact operator values are computed at those points and stored. The exact evaluation of the operators also requires the solution of thermodynamic equilibrium problem. We employ the multiphase flash [47] for the evaluation of instantaneous thermodynamic equilibrium between fluid phases, implemented in DARTS-flash package [60]. Once operators have been evaluated at a certain point, they are stored in a multidimensional table and can be used for the evaluation of operators and their derivatives in adjacent hypercubes.

2.5. Solution strategy

Solving the system of $n_c + 4$ nonlinear discrete Eq. (19) involves significant computational challenges. We utilize Newton-Raphson iterations to resolve nonlinearities. Linear systems appearing in these iterations can not be handled efficiently with direct solvers already for grids comprised of more than 10^4 cells. Therefore, the scalable iterative linear solution strategy is required for the integration of realistic models.

In this work, we implement the two-stage block-partitioned preconditioning strategy for multiphase poromechanics [23]. The strategy exploits the fixed-stress approximation, which has been initially developed for the sequential solution of poromechanical systems [21], and later has been successfully utilized in the preconditioning of fully implicit systems [33].

In the first stage, this preconditioning strategy considers the block-partitioned system

$$
\mathbf{U}^{-1}\mathbf{J}\begin{bmatrix}\boldsymbol{\delta\omega}\\\boldsymbol{\delta u}\end{bmatrix}=\begin{bmatrix}\mathbf{I} & -\mathbf{J}_{\omega u}\mathbf{J}_{uu}^{-1}\\ \mathbf{0} & \mathbf{I}\end{bmatrix}\begin{bmatrix}\mathbf{J}_{\omega\omega} & \mathbf{J}_{\omega u}\\ \mathbf{J}_{u\omega} & \mathbf{J}_{uu}\end{bmatrix}\begin{bmatrix}\boldsymbol{\delta\omega}\\\boldsymbol{\delta u}\end{bmatrix}=\begin{bmatrix}\mathbf{S}_{\omega} & \mathbf{0}\\ \mathbf{J}_{u\omega} & \mathbf{J}_{uu}\end{bmatrix}\begin{bmatrix}\boldsymbol{\delta\omega}\\\boldsymbol{\delta u}\end{bmatrix}=-\begin{bmatrix}\mathbf{H}_{\omega}-\mathbf{J}_{\omega u}\mathbf{J}_{uu}^{-1}\mathbf{H}_{u}\\ \mathbf{H}_{u}\end{bmatrix},
\tag{67}
$$

where $\mathbf{J}$ is the Jacobian matrix, $[\boldsymbol{\delta\omega},\boldsymbol{\delta u}]^{T}=[\boldsymbol{\delta p},\boldsymbol{\delta z},\boldsymbol{\delta\Theta},\boldsymbol{\delta u}]^{T}$ is the vector of unknown increments of pressures, compositions, temperatures for non-isothermal systems, and displacements, respectively, the jacobian subblock $\mathbf{J}_{ab}$ denote the derivatives of residual of equation a with respect to primary unknown b assembled across all cells, while $\mathbf{H}_{\omega}$ and $\mathbf{H}_{u}$ are the vectors of residuals in corresponding mass-energy and momentum discrete balance equations, respectively. Note that here we group state unknowns $\boldsymbol{\delta\omega}=[\boldsymbol{\delta p},\boldsymbol{\delta z},\boldsymbol{\delta\Theta}]^{T}$, corresponding mass and energy equations and treat them equally in the first stage. The Schur complement $\mathbf{S}_{\omega}$ of block $\mathbf{J}_{uu}$ in the Jacobian is equal to

$$
\mathbf{S}_{\omega}=\begin{bmatrix}\mathbf{J}_{pp}-\mathbf{J}_{pu}\mathbf{J}_{uu}^{-1}\mathbf{J}_{up} & \mathbf{J}_{pz}-\mathbf{J}_{pu}\mathbf{J}_{uu}^{-1}\mathbf{J}_{uz} & \mathbf{J}_{p\theta}-\mathbf{J}_{pu}\mathbf{J}_{uu}^{-1}\mathbf{J}_{u\theta}\\ \mathbf{J}_{zp}-\mathbf{J}_{zu}\mathbf{J}_{uu}^{-1}\mathbf{J}_{up} & \mathbf{J}_{zz}-\mathbf{J}_{zu}\mathbf{J}_{uu}^{-1}\mathbf{J}_{uz} & \mathbf{J}_{z\theta}-\mathbf{J}_{zu}\mathbf{J}_{uu}^{-1}\mathbf{J}_{u\theta}\\ \mathbf{J}_{\theta p}-\mathbf{J}_{\theta u}\mathbf{J}_{uu}^{-1}\mathbf{J}_{up} & \mathbf{J}_{\theta z}-\mathbf{J}_{\theta u}\mathbf{J}_{uu}^{-1}\mathbf{J}_{uz} & \mathbf{J}_{\theta\theta}-\mathbf{J}_{\theta u}\mathbf{J}_{uu}^{-1}\mathbf{J}_{u\theta}\end{bmatrix},
\tag{68}
$$

and can be approximated by $\tilde{\mathbf{S}}_{\omega}$ defined as

$$
\tilde{\mathbf{S}}_{\omega}=\begin{bmatrix}\mathbf{J}_{pp}-\mathrm{diag}(\mathbf{J}_{pu}\mathbf{J}_{uu}^{-1}\mathbf{J}_{up}\mathbf{e}) & \mathbf{J}_{pz} & \mathbf{J}_{p\theta}\\ \mathbf{J}_{zp}-\mathrm{diag}(\mathbf{J}_{zu}\mathbf{J}_{uu}^{-1}\mathbf{J}_{up}\mathbf{e}) & \mathbf{J}_{zz} & \mathbf{J}_{z\theta}\\ \mathbf{J}_{\theta p}-\mathrm{diag}(\mathbf{J}_{\theta u}\mathbf{J}_{uu}^{-1}\mathbf{J}_{up}\mathbf{e}) & \mathbf{J}_{\theta z} & \mathbf{J}_{\theta\theta}\end{bmatrix},
\tag{69}
$$

where row-sum lumping strategy is utilized , $\mathbf{e}=[1,\cdots,1]^{T}$ is a probing vector and diag() denotes a diagonal matrix constructed from an input vector. This lumping strategy is an algebraic generalization of fixed-stress approximation [34] recalling the probing technique for computing Schur complements [61]. For the evaluation of $\mathbf{J}_{uu}^{-1}$ we use a single V-cycle of algebraic multigrid (AMG) solver that provides a good approximation to this matrix.

The rationale behind the simplifications introduced by Eq. (69), specifically the assumptions $\mathbf{J}_{uz}\approx 0$ and $\mathbf{J}_{u\theta}\approx 0$, is as follows. The subblock $\mathbf{J}_{uz}$ captures the influence of fluid composition on the momentum balance through their effect on density multiplier in gravitational forces. Practically, variations in fluid composition have a little effect on the overall density of saturated rocks, which justifies neglecting this coupling. Consequently, for consistency, $\mathbf{J}_{u\theta}$ is also eliminated. This is explained by the treatment of temperature as a hyperbolic variable, along with fluid compositions, in the second stage of the preconditioner. The neglect of $\mathbf{J}_{u\theta}$ maintains the consistency among hyperbolic variables offloading the second-stage preconditioner. Note, however, that the conduction-dominated regimes may require retaining $\mathbf{J}_{u\theta}$ in the approximation of Schur complement.

In contrast to Finite Element Method, the multi-point stress approximation (MPSA) used in this paper does not produce a symmetric positive-definite (SPD) matrix $\mathbf{J}_{uu}$ that can compromise the efficiency of multigrid solvers. Related convergence analysis and theoretical guarantees for non-symmetric systems are limited by the systems with dominated SPD part [62,63]. Nonetheless, multigrid solvers reportedly demonstrate their efficiency for a wider classes of matrices beyond SPD [64,65]. More importantly, they exhibit notable efficiency in solving non-symmetric systems arising from the discretization of elliptic-dominated operators of fluid flow and transport problems [66] as well as coupled poroelasticity models [67] in reservoir engineering. Although a few symmetric positive-definite MPFA schemes have been proposed [68,69], constructing a symmetric MPSA scheme presents greater challenges. Potential approaches include weakly imposing the symmetry of the stress tensor [70] or adopting mixed displacement-stress formulation, which can be constructed in analogy to diffusion operator [71].

In the second stage, the Constrained Pressure Residual (CPR) preconditioner [72,73] can be used to find an approximate solution for the multiphase flow system. CPR preconditioner also performs in two stages. In the first stage, the system is divided into pressure (elliptic) and composition-temperature (hyperbolic) subsystems with True-IMPES (implicit-pressure explicit-saturation) reduction algorithm [74]. The pressure subsystem is solved with an AMG solver and often a single V-cycle provides an accurate enough solution. In the second stage of the CPR preconditioner, the multiphase flow system with substituted pressure solution is subjected to the Incomplete LU (ILU) preconditioner. The described CPR preconditioner has proven to be robust and efficient in accelerating the modeling of a wide range of geo-energy applications [73,75]. Although, the standard CPR considers only fluid composition (or saturation) as hyperbolic unknowns, in some cases, it can efficiently handle systems obtained in geothermal modeling by treating temperature unknown and energy balance as a part of the hyperbolic subsystem [75]. However, dominant heat conduction regimes can compromise its efficiency and, generally, the extended CPTR preconditioner must be employed [76,77].

The described preconditioner is summarized in Algorithm 1, where $\mathcal{P}_{u}^{-1}$ is a single V-cycle of BoomerAMG [78], tuned for three-dimensional elasticity problem, $\mathcal{P}_{\omega}^{-1}$ is an in-house implementation of CPR preconditioner [75].

3. Results

3.1. Convergence study

Convergence study of the system of Eqs. (1)–(3) is complicated by a few nonlinearities. Nonlinearities do not allow to perform a general measurement of convergence rate as it becomes case-dependent. Therefore, we have to introduce a couple of simplifications linearizing thermo-poroeasticity system to perform a rigorous measurements of convergence rate. First, it is possible to investigate convergence only for single-phase slightly compressible flow as multiphase compositional flow introduces unavoidable

---

Algorithm 1 Nonlinear iteration.

1: **procedure** NONLINEAR_ITERATION($\mathbf{J}, \mathbf{H}$, tol, max_iter)   ▷ Newton-Raphson
2:     $\mathcal{P}_u^{-1}, \mathcal{P}_\omega^{-1} \leftarrow$ PRECONDITIONER_SETUP($\mathbf{J}, \mathbf{H}$)
3:     **for** $j = 0 \ldots$ max_iter $- 1$ **do**   ▷ GMRES iterations
4:        $\widetilde{\delta\omega}, \widetilde{\delta\mathbf{u}} \leftarrow$ PRECONDITIONER_SOLVE($\mathbf{J}, \mathbf{H}, \mathcal{P}_u^{-1}, \mathcal{P}_\omega^{-1}$)   ▷ Initial guess
5:        MGS_ORTHOGONALIZATION   ▷ Modified Gram-Schmidt
6:        ARNOLDI_STEP
7:        $\delta\omega, \delta\mathbf{u}$, res $\leftarrow$ UPDATE($\widetilde{\delta\omega}, \widetilde{\delta\mathbf{u}}$)
8:        **if** res $<$ tol **then**
9:           Break
10:    **return** $\delta\omega, \delta\mathbf{u}$, res
11:
12: **procedure** PRECONDITIONER_SETUP($\mathbf{J}, \mathbf{H}$)
13:     Setup $\mathcal{P}_u^{-1}(\mathbf{J}_{uu})$ ▷ $\mathcal{P}_u^{-1}$ – V-cycle of BoomerAMG
14:     $\mathbf{e} \leftarrow [1, \cdots, 1]^T$
15:     $\tilde{\mathbf{S}}_\omega \leftarrow \begin{bmatrix} \mathbf{J}_{pp} - \operatorname{diag}(\mathbf{J}_{pu}\mathcal{P}_u^{-1}\mathbf{J}_{up}\mathbf{e}) & \mathbf{J}_{pz} & \mathbf{J}_{p\theta} \\ \mathbf{J}_{zp} - \operatorname{diag}(\mathbf{J}_{zu}\mathcal{P}_u^{-1}\mathbf{J}_{up}\mathbf{e}) & \mathbf{J}_{zz} & \mathbf{J}_{z\theta} \\ \mathbf{J}_{\theta p} - \operatorname{diag}(\mathbf{J}_{\theta u}\mathcal{P}_u^{-1}\mathbf{J}_{up}\mathbf{e}) & \mathbf{J}_{Tz} & \mathbf{J}_{\theta\theta} \end{bmatrix}$
16:     Setup $\mathcal{P}_\omega^{-1}(\tilde{\mathbf{S}}_\omega)$ ▷ $\mathcal{P}_\omega^{-1}$ – CPR
17:     **return** $\mathcal{P}_u^{-1}, \mathcal{P}_\omega^{-1}$
18:
19: **procedure** PRECONDITIONER_SOLVE($\mathbf{J}, \mathbf{H}, \mathcal{P}_u^{-1}, \mathcal{P}_\omega^{-1}$)
20:     $\delta\omega \leftarrow \mathcal{P}_\omega^{-1}\left(-\mathbf{H}_\omega + \mathbf{J}_{\omega u}\mathcal{P}_u^{-1}\mathbf{H}_u\right)$
21:     $\delta\mathbf{u} \leftarrow \mathcal{P}_u^{-1}\left(-\mathbf{H}_u - \mathbf{J}_{u\omega}\delta\omega\right)$
22:     **return** $\delta\omega, \delta\mathbf{u}$

---

nonlinearities compromising the measurement of convergence rate. Specifically, the effective density, internal energy and heat conduction averaged over fluid and rock matrix introduce additional nonlinearities in the system. For this study, we simplify these terms as

$$(1 - \phi)\rho_s + \phi \sum_\alpha^{n_p} S_\alpha \rho_\alpha \to \rho_{\text{tot}}, \tag{70}$$

$$(1 - \phi)\rho_s U_s + \phi \sum_\alpha^{n_p} S_\alpha \rho_\alpha U_s \to h_{\text{tot}} = c\Theta, \tag{71}$$

$$(1 - \phi)\mathbf{q}_s^\theta + \sum_\alpha^{n_p} \phi S_\alpha \mathbf{q}_\alpha^\theta \to \mathbf{q}_{\text{tot}}^\theta = -\mathbf{\Lambda}\nabla\Theta, \tag{72}$$

where ρ_{tot} is a constant, h_{tot} and the approximated $\mathbf{q}_{\text{tot}}^\theta$ are linear functions of unknowns, with constant heat capacity c and heat conductivity tensor $\mathbf{\Lambda}$. Note that Eq. (71) neglects the thermoporoelastic effect on temperature through porosity changes with alternating pressure and temperature.

Despite these simplifications, the heat convection in Eq. (2) maintains the system nonlinear. To overcome this nonlinearity, we perform two convergence studies: the first one investigates the convergence of a poroelastic system without energy balance while the second, thermoporoelastic, one considers a linear pressure distribution which allows the convergence of the system to be estimated in the presence of heat convection. The linearity-preserving property of these numerical schemes [13,16] enables the machine-precision approximation of linearly distributed unknowns across a domain. As a result, Darcy's fluxes enjoy a much more accurate approximation compared to the enthalpy multiplier defined by nonlinearly distributed temperature across the domain. This explains the possibility of measuring the convergence rate in the second study.

Consider a cubic domain $\Omega = [0, a]^3$ of a side length $a = 1\,\text{m}$ with the following constant stiffness matrix $\mathbf{C}$, Biot tensor $\mathbf{B}$, permeability tensor $\mathbf{K}$, thermal dilation tensor $\mathbf{A}$ and heat conductivity tensor $\mathbf{\Lambda}$:

$$\mathbf{C} = \begin{bmatrix} 1.323 & 0.0726 & 0.263 & 0.108 & -0.08 & -0.239 \\ 0.0726 & 1.276 & -0.318 & 0.383 & 0.108 & 0.501 \\ 0.263 & -0.318 & 0.943 & -0.183 & 0.146 & 0.182 \\ 0.108 & 0.383 & -0.183 & 1.517 & -0.0127 & -0.304 \\ -0.08 & 0.108 & 0.146 & -0.0127 & 1.209 & -0.326 \\ -0.239 & 0.501 & 0.182 & -0.304 & -0.326 & 1.373 \end{bmatrix} \text{[bar]},$$

$$\mathbf{B} = \begin{bmatrix} 1.5 & 0.1 & 0.5 \\ 0.1 & 1.5 & 0.15 \\ 0.5 & 0.15 & 1.5 \end{bmatrix}, \quad \mathbf{K} = \begin{bmatrix} 1.5 & 0.5 & 0.35 \\ 0.5 & 1.5 & 0.45 \\ 0.35 & 0.45 & 1.5 \end{bmatrix} \text{[mD]},$$

Table 2
The remaining properties used in the convergence studies.

Property	Value	Unit
Porosity, ϕ_0	0.1	–
Fluid density, ρ_f	978	$\mathrm{kg\,m^{-3}}$
Fluid viscosity, μ_f	0.01	cP
Fluid compressibility, β_f	0	$\mathrm{bar^{-1}}$
Total density, ρ_{tot}	2482.8	$\mathrm{kg\,m^{-3}}$
Rock compressibility, β_s	1.4503768×10^{-6}	$\mathrm{bar^{-1}}$
Gravitational acceleration, g	0.0981	$\mathrm{m\,d^{-2}}$
Heat capacity, c	1	$\mathrm{kJ\,m^{-3}\,K^{-1}}$

$$\mathbf{A} = \begin{bmatrix} 1.5 & 0.5 & 0.35 \\ 0.5 & 1.5 & 0.45 \\ 0.35 & 0.45 & 1.5 \end{bmatrix} [\mathrm{bar\,K^{-1}}], \qquad \mathbf{\Lambda} = \alpha \begin{bmatrix} 1.5 & 0.1 & 0.5 \\ 0.1 & 1.5 & 0.15 \\ 0.5 & 0.15 & 1.5 \end{bmatrix} [\mathrm{Wm^{-1}K^{-1}}],$$

where α denotes an input parameter used to measure the convergence rate for various Peclet numbers. The remaining properties are listed in Table 2.

Let us consider the reference solution for displacements defined as

$$u(x, y, z, t) = \left[(x - 0.5)^2 - y - z\right](1 + t^2),$$
$$v(x, y, z, t) = \left[(y - 0.5)^2 - x - z\right](1 + t^2),$$
$$w(x, y, z, t) = \left[(z - 0.5)^2 - x - y\right](1 + t^2). \tag{73}$$

Additionally, let us define the following nonlinear function

$$f(x, y, z, t) = \frac{1}{2\sin(1)} \sin((1 - x)(1 - y)(1 - z)) + 0.5(1 - x)^3(1 - y)^2(1 - z)(1 + t^2). \tag{74}$$

In the first convergence study, we estimate the convergence rate for the poroelastic system. For this purpose we utilize the function from Eq. (74) as a pressure reference solution, i.e. $p = f$. Neither energy balance nor thermal dilation are considered in this study. Subsequently, the reference displacement and pressure solutions are substituted to fluid mass and momentum balance Eqs. (1) and (3); and the respective right-hand sides of these equations are calculated for every cell at every time step. These values are substituted to the numerical scheme as free terms. Besides, the reference solution defines Dirichlet boundary conditions, applied to fluid and momentum balance equations. As a result, the numerical scheme must approximate the given reference solution.

Fig. 3 demonstrates the L2 error norms between reference $p, \mathbf{u}$ and numerical $p_h, \mathbf{u}_h$ solutions against spatiotemporal resolution. The norms for arbitrary quantity A and its discrete approximation A_h are calculated as follows:

$$\|A - A_h\| = \sqrt{\left(\sum_i i\right)^{-1} \sum_i i |A(\mathbf{x}_i) - A_{h,i}|^2}, \tag{75}$$

(a) cubic grid (b) tetrahedral grid
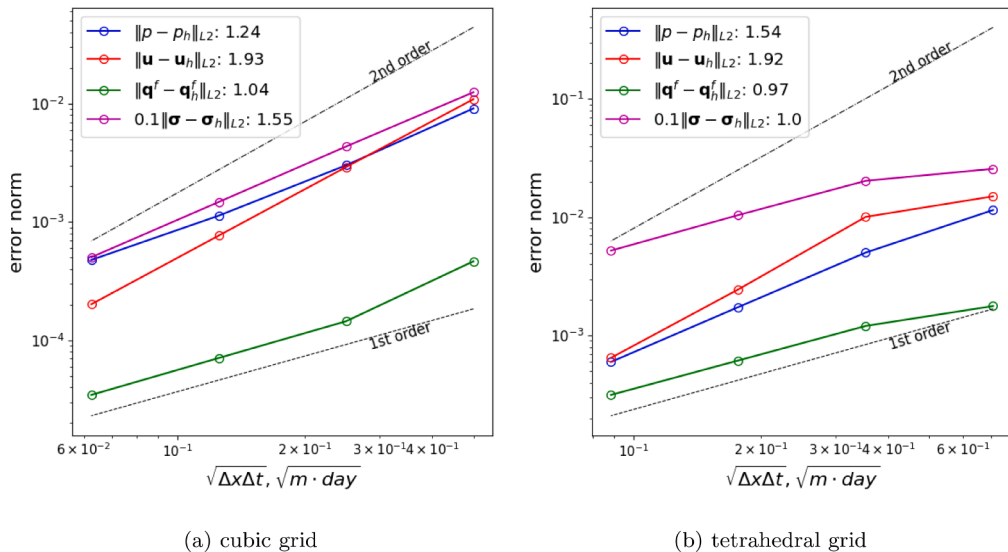
Fig. 3. The L2 error norm against space-time resolution obtained with cubic (a) and tetrahedral (a) grids.

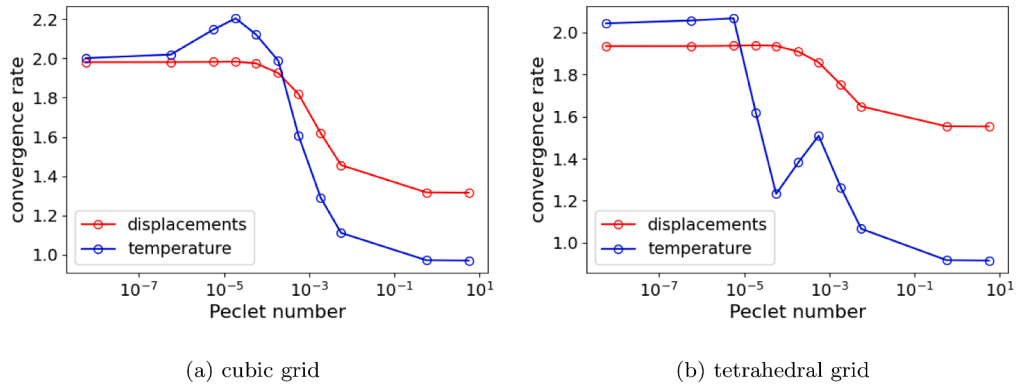(a) cubic grid   (b) tetrahedral grid

Fig. 4. The sensitivity of numerical convergence rate to the Peclet number of heat transfer investigated with cubic (a) and tetrahedral (a) grids.

Table 3
The properties of two layers in the two-layer Terzaghi setup.

Layer	h, m	E, GPa	v	b	k, mD	ϕ_0	μ_f, cP	β_f, bar^{-1}
1	25	1	0.35	0.9	1	0.15		
2	75	5	0.0053	0.01	0.001	0.00656	1	10^{-10}

where i denotes the volume of i-th cell, $\mathbf{x}_i$ – its center. In the norm evaluation, the stress tensor is treated as a vector of six components, written in Voigt notations. The results are obtained with a series of cubic and tetrahedral grids composed of 8^2, 8^3, 8^4, 8^5 cubes and 100, 384, 2604, 18,921 tetrahedrons, respectively. As it was shown before [13,16], displacements demonstrate a nearly quadratic convergence rate while pressure, which suffers from the first-order approximation of time derivatives, exhibits only a super-linear convergence rate. Additionally, Fig. 3 illustrates a linear convergence rate of Darcy's velocities $\mathbf{q}_h^f$ and stress tensors σ_h reconstructed at cell centers.

In the second convergence study, we estimate the convergence rate for the thermoporoelastic system. To avoid the nonlinearity of convective fluxes in energy balance, we employ the following time-independent reference solution for pressure

$$p(x, y, z, t) = 3 - x - y - z, \tag{76}$$

which represents a linear function in space. Linearity-preserving property of the scheme [13] delivers machine precision to the pressure solution, which allows the convergence with respect to other unknowns to be consistently measured. Temperature is defined by the reference solution from Eq. (74), i.e. $\Theta = f$, while the reference solutions for displacements remain defined according to Eq. (73). Following the same procedure as in the first study, we incorporate these reference solutions into the numerical calculations.

Fig. 4 presents the measured convergence rate of displacements and temperature against Peclet number Pe $= \dfrac{ac\|\mathbf{q}^f\|_{L2}}{\|\mathbf{\Lambda}\|_{L2}}$. It shows that in conduction-dominated region we obtain a second order of convergence for both displacements and temperature. For higher Peclet numbers, the convergence weakens up to super-linear for displacements and linear for temperature at convective-dominated limit. This behavior is expected as the scheme respect the balance of heat conduction fluxes in Eq. (26).

Note that in reservoir conditions, the Peclet number can reach values of $\sim 10^3$ magnitude near wells. According to Fig. 4, this can significantly hampers the ability to achieve a quadratic convergence rate and, in turn, accurate enough, converged solutions on moderate meshes. This underscores the necessity of highly resolved meshes and efficient preconditioning techniques for handling associated large linear systems to ensure obtaining converged results.

3.2. Uniaxial poroelastic consolidation (Terzaghi's problem)

We further validate the numerical scheme against the analytical solution for the unidimensional consolidation problem, also known as Terzaghi's problem. As the analytical solution in the presence of the two heterogeneous layers in Terzaghi's problem remains feasible [31,79], we consider this more general setup. The poroelastic domain shown in Fig. 5 of vertical extent $h = 100$ m is comprised by two layers of distinct properties with $h_1 = 25$ m, $h_2 = 75$ m respectively. The first layer is adjacent to the right boundary which is subjected to constant normal load $F = 10$ MPa and constant initial pressure $p_0 = 0$ Pa. All other sides of the domain are impermeable to fluid and subjected to the roller boundary condition (normal displacement and tangential traction are equal to zero). The domain's permeabilities $\mathbf{K} = k\mathbf{I}$ and Biot's tensors $\mathbf{B} = b\mathbf{I}$ are defined by their scalar counterparts k and b, respectively, while the stiffness tensors are determined by Young's moduli E and Poisson's ratios v. The properties of porous matrix and fluid including initial porosities ϕ_0, fluid viscosity μ_f and fluid compressibility β_f are listed in Table 3.

The comparison of results is presented in Fig. 6. We use a uniform mesh comprised of 40 cells, so that the top left subfigure (Fig. 6(a)) demonstrates pressure over time evaluated at $x = 1.25$ m and the bottom left subfigure (Fig. 6(c)) shows the dynamics of horizontal displacement u$_x$ taken at $x = 98.75$ m. The top and bottom right subfigures (Fig. 6(b), Fig. 6(d)) present pressure and
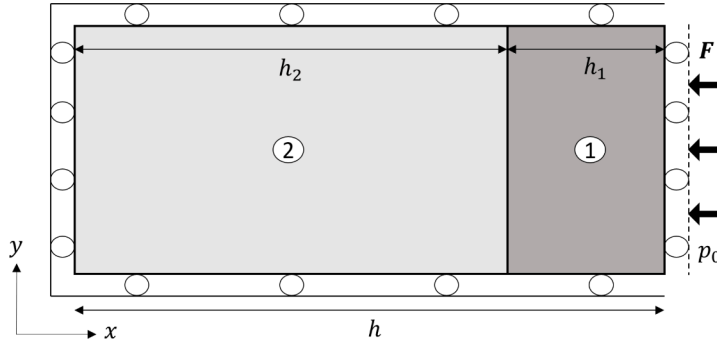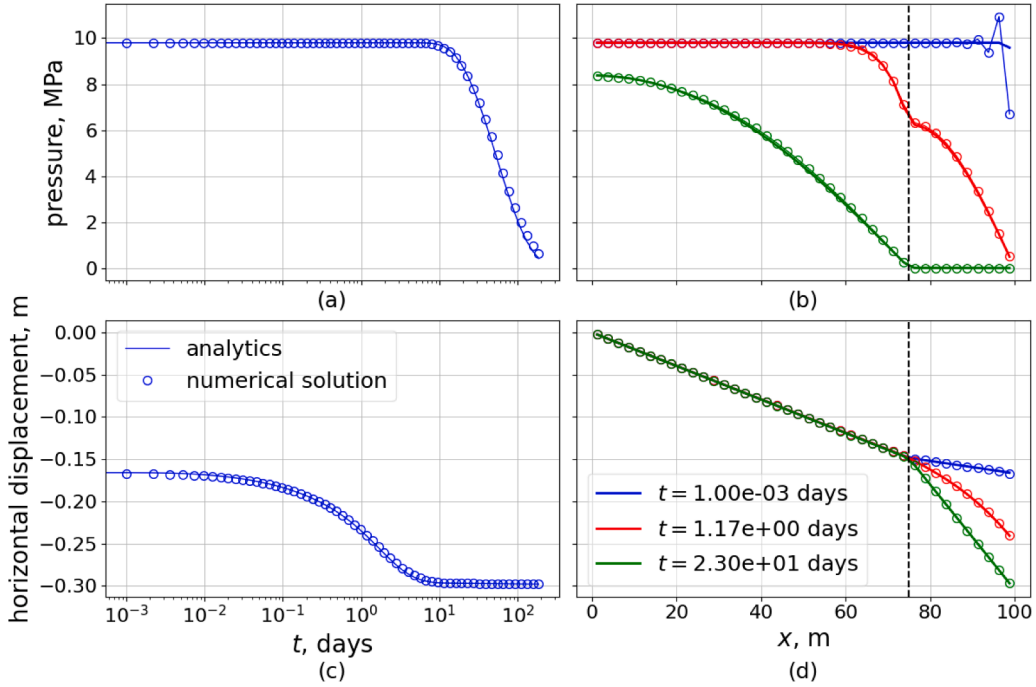
Fig. 5. Two-layer Terzaghi setup.

Fig. 6. Comparison of the analytical and numerical solutions for the two-layer Terzaghi's problem. In the left column, pressure (a) and displacement (c) at the center of the most left cell are shown over time. In the right column, pressure (b) and displacement (d) profiles over the whole domain are depicted at three moments of time.

horizontal displacement profiles over the domain respectively. Numerical results remain in good accordance with the analytical solution. For the simplicity of analytical solution, we assume the Skempton's coefficient is equal in both layers. As a result, the compression of the poroelastic domain causes an instant pressure build-up, uniform throughout the whole domain. The thin boundary layer originates at the right side of the domain subjected to the constant initial pressure. Numerically it produces spurious oscillations that disappear over time. They can be observed in Fig. 6(b). These oscillations indicate the inf-sup instability of the scheme [24,25], which can be overcome by introducing regularization [80], by choosing the essentially inf-sup stable discretization spaces [30] or by using flux vector splitting [31]. The analysis of the latter approach applied to the current scheme is conducted in [32].

We conducted the convergence study for homogeneous domain covered by uniform rectangular mesh. Fig. 7 demonstrates a decay of discrepancy between analytical and numerical solutions in terms of L2 norm defined in Eq. (75) and evaluated at $T = 10$ d. At the finest resolution of 1500 cells and 1500 time steps, the solutions evaluated at $t = 10$ d demonstrate the maximum relative differences 0.009 % and 0.01 % for pressure and displacement fields, respectively. The linear convergence rate observed in Fig. 7 is lower than reported in Section 3.1. This can be explained by perturbations introduced by inf-sup instability at the beginning of simulation and unavoidable round-off errors.
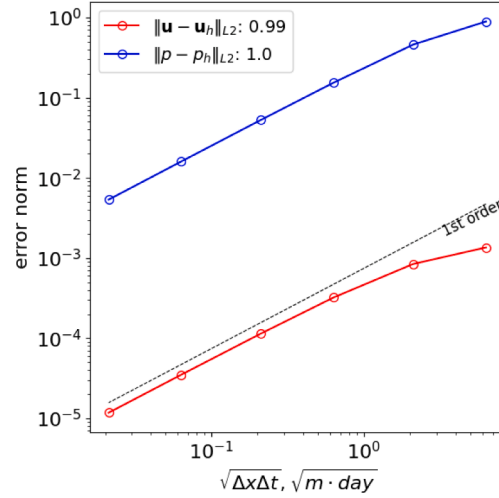
Fig. 7. The L2 error norm of difference between analytical and numerical solutions against space-time resolution.
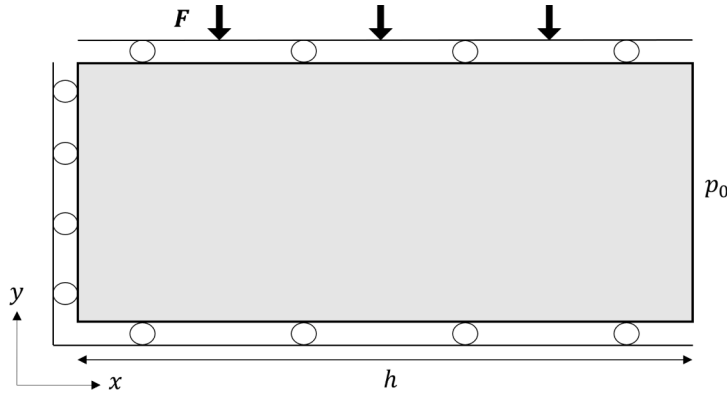

Fig. 8. Mandel setup.

3.3. Biaxial poroelastic consolidation (Mandel's problem)

Consider the same domain as in the previous section with homogeneous properties and different boundary conditions illustrated in Fig. 8. Now roller boundary conditions are applied only to the left and bottom boundaries of the domain. The right boundary is free of both normal and tangential forces while a normal load is applied from the top. Note that this load is applied through the stiff bulk in a way that produces uniform vertical displacement. Therefore, it could be more convenient to specify time-dependent normal displacement at the top estimated from analytical expressions. No-flow conditions are specified for all boundaries except for the right one subjected to the Dirichlet condition $p_0 = 0$ Pa. This setup is the so-called Mandel's problem which is often used as an example of non-monotonic pressure behavior following undrained loading.

A porous homogeneous domain is characterized by Young's modulus E = 1 GPa, Poisson's ratio $v = 0.25$, a diagonal permeability tensor $\mathbf{K} = k\mathbf{I}, k = 1$ mD, saturated with a single-phase compressible fluid with compressibility $\beta_f = 10^{-10}$ bar^{-1}, viscosity $\mu_f = 1$ cP, and with a Biot modulus M = 10^{-5} bar^{-1} and a diagonal Biot tensor $\mathbf{B} = b\mathbf{I}, b = 0.9$.

For the numerical solution, we use 30×30 square mesh. Fig. 9 depicts a comparison between the numerical solution and analytics [31,79]. As in the previous section, the top left subfigure (Fig. 9(a)) shows the pressure dynamics evaluated at $x = 1.66$ m, the bottom left subfigure (Fig. 9(c)) shows the dynamics of horizontal displacement u_x at $x = 98.33$ m, the right top (Fig. 9(b)) and right bottom (Fig. 9(d)) subfigures illustrate the profiles of pressure and vertical displacement correspondingly over horizontal centerline at three moments of time. The numerical solution matches analytics quite well. As in the previous example, spurious oscillations arise around the right side of the domain at the very beginning of simulation. They can be seen in the top right subfigure (Fig. 9(b)).

We conducted the convergence study for homogeneous domain covered by uniform rectangular mesh. Fig. 10 demonstrates a decay of discrepancy between analytical and numerical solutions in terms of L2 norm defined in Eq. (75) and evaluated at $T = 10$ d. At the finest resolution of 1500 cells per x-axis and 1500 time steps, the solutions evaluated at $t = 10$ d demonstrate the maximum relative differences 0.007 % and 0.002 % for pressure and displacement fields, respectively. The linear convergence rate observed in
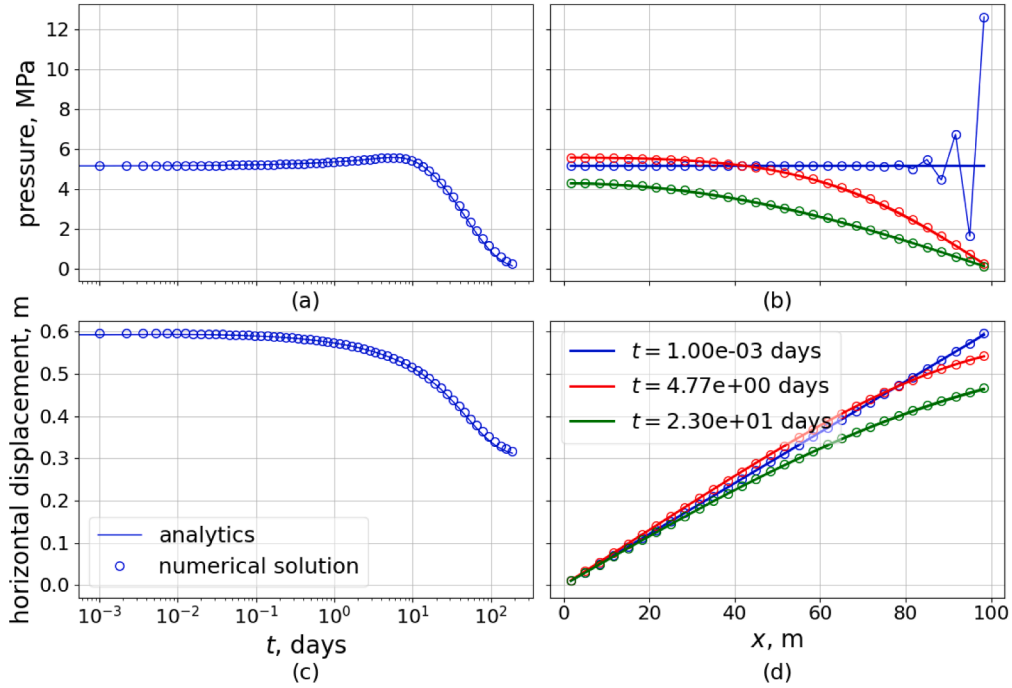
Fig. 9. Comparison of the analytical and numerical solutions for Mandel's problem. In the left column, pressure (a) and displacement (c) at the center of the most left cell are shown over time. In the right column, pressure (b) and displacement (d) profiles over the whole domain are depicted at three moments of time.
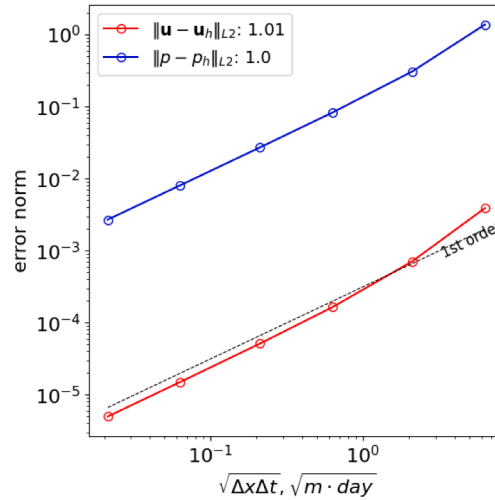
Fig. 10. The L2 error norm of difference between analytical and numerical solutions against space-time resolution.

Fig. 10 is lower than reported in Section 3.1. This can be explained by perturbations introduced by inf-sup instability at the beginning of simulation and unavoidable round-off errors.

3.4. Uniaxial thermoporoelastic consolidation

The semi-analytical solution for a coupled problem of fluid mass, energy, and momentum balance in the uniaxial consolidation test [82] can be employed to benchmark the developed scheme. Thus, we consider the vertical column of $7\,\mathrm{m}$ height subjected to instant vertical loading with $F = 1\,\mathrm{Pa}$ at the top boundary [81]. The constant pressure $\mathrm{p} = 0\,\mathrm{Pa}$ and temperature $\Theta = 50\,°\mathrm{C}$ is maintained at the top boundary while the initial pressure and temperature are equal to $p_0 = 0\,\mathrm{Pa}$ and $\Theta_0 = 0\,°\mathrm{C}$, respectively. All other sides of the domain are impermeable to fluid and heat and subjected to the roller boundary condition. The domain is shown in Fig. 11.
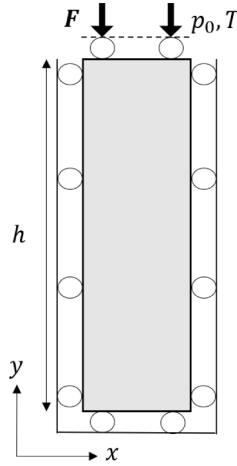
Fig. 11. The setup for uniaxial thermoporoelastic consolidation test [81].

(a) pressure

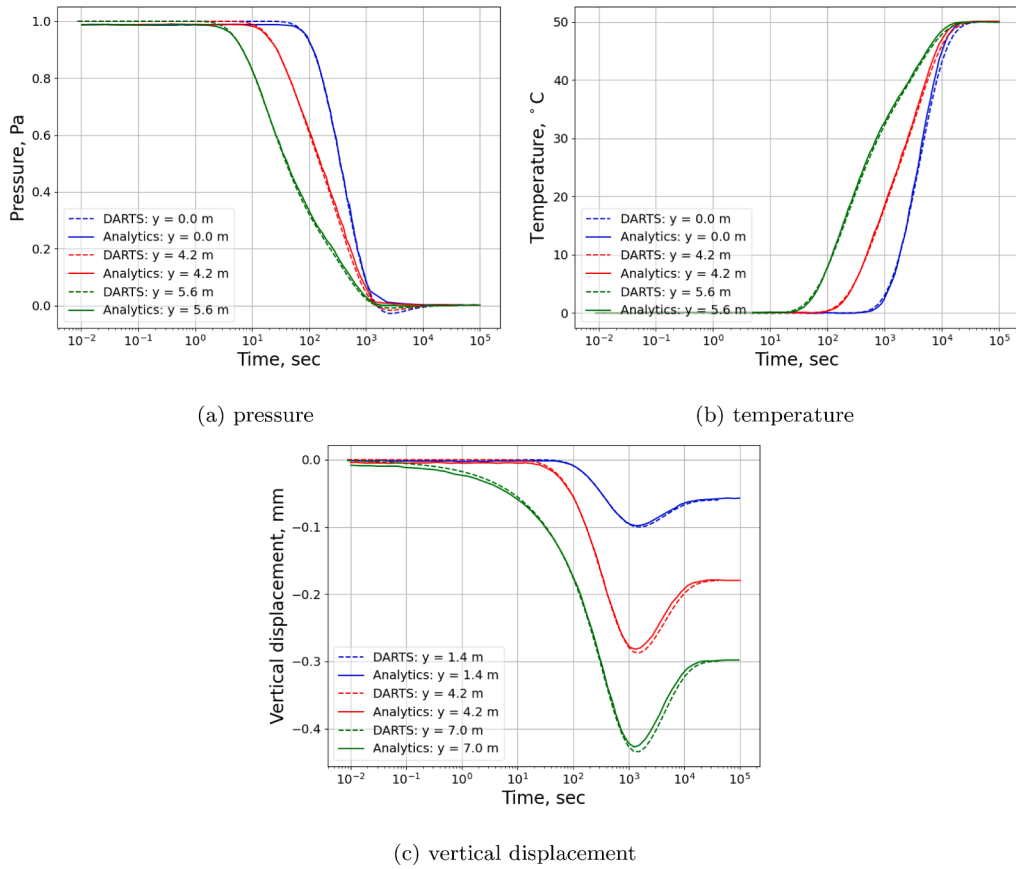(b) temperature

(c) vertical displacement

Fig. 12. The dynamics of pressure (a), temperature (b) and vertical displacement (c) over time estimated in three points in space with semi-analytical method and DARTS.

Furthermore, the stiffness tensor is defined by Young's modulus $E = 6\,\text{kPa}$ and Poisson's ratio $\nu = 0.4$. Isotropic permeability $\mathbf{K} = k\mathbf{I}$, Biot's $\mathbf{B} = b\mathbf{I}$, thermal dilation $\mathbf{A} = a\mathbf{I}$ and total heat conduction $\mathbf{\Lambda} = \lambda\mathbf{I}$ tensors are defined by the corresponding scalar values $k = 4 \times 10^{-9}\,\text{m}^2$, $b = 1.0$, $a = 9 \times 10^{-7}\,°\text{C}^{-1}$ and $\lambda = 836\,\text{Jm}^{-1}\,\text{s}^{-1}\,°\text{C}^{-1}$, respectively. The total volumetric heat capacity is equal to $c = 167.2\,\text{kJm}^{-3}\,°\,\text{C}^{-1}$. Fluid is maintained incompressible with fluid viscosity $\mu = 1\,\text{cP}$.

Fig. 12 illustrates the comparison of pressure, temperature, and vertical displacement to the analytical solution. Pressure, temperature, and vertical displacement evaluated at three points in space are plotted against time. The numerical solution obtained with the proposed scheme (DARTS) demonstrates a good match to the semi-analytical solution (Analytics).
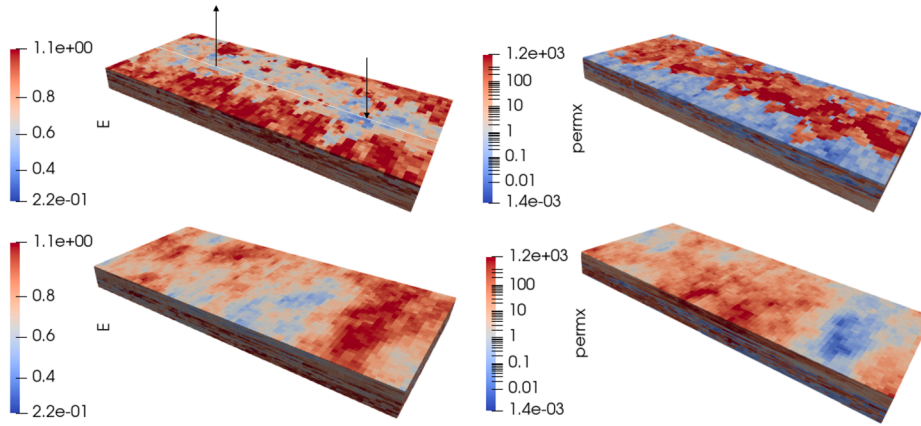
Fig. 13. Young modulus (in tens of GPa) and lateral permeability (in mD) fields shown from the top (top row) and from the bottom (bottom row) of reservoir. Young's modulus is calculated as a linear function of porosity.

Table 4
The description of fluid physics used in the study.

Property	Single-phase	Two-phase
Phase densities, $kg\,m^{-3}$	666.85	1014, 50
Phase compressibilities, bar^{-1}	1.45×10^{-5}	$10^{-5}, 5 \times 10^{-3}$
Phase viscosities, cP	1.0	0.3, 0.03
Phase relative permeabilities,	–	$\left(\frac{S_a - 0.1}{1 - 0.2}\right)^2$
Phase heat capacities, $kJkg^{-1}°C^{-1}$	–	4.18, 0.035
Initial phase saturation	1	0.67, 0.33

An instant loading causes an instant compression followed by further consolidation due to fluid discharge as in the uniaxial poroelastic consolidation test. However, heat conduction propagates energy from the top boundary, which is maintained under high temperature $\Theta = 50\,°C$, throughout the whole domain. Temperature increase causes thermal expansion, competing with consolidation.

### 3.5. Thermoporoelastic extension of SPE10 model

This field-scale test case utilizes a reservoir model from the 10th SPE Comparative Solution Project (SPE10). Following [19], we extend this model with mechanical properties to perform a coupled compositional modeling in heterogeneous thermo-poroelastic medium.

The original project's model is covered with a regular Cartesian $60 \times 220 \times 85$ grid that spans two formations: the top 50 layers have a channelized permeability distribution while the bottom 35 layers represent a permeability field that has a Gaussian spatial covariance. Mechanical properties are defined by heterogeneous Young's modulus linearly dependent on porosity, uniform Poisson's ratio $\nu = 0.2$, Biot's coefficient $b = 1$, thermal expansion coefficient $\alpha = 9 \cdot 10^{-7} °C^{-1}$. The reservoir has a uniform rock density $\rho_s = 2650\,kg\,m^{-3}$, rock heat capacity $c_s = 2.2\,kJkg^{-1}°C^{-1}$ and effective heat conductivity $\lambda_0 = 72.23\,kJm^{-1}d^{-1}°C^{-1}$. Fig. 13 shows the corresponding Young's modulus E and x-axis permeability k_x maps. For the scalability study, we coarsened the original model using a volume-averaging approach [19]. The domain is subjected to impermeable boundary conditions and constant temperature defined by the temperature at top $\Theta_{top} = 26.85°C$ and bottom $\Theta_{bot} = 76.85°C$ of domain distributed between according to a constant geothermal gradient. Furthermore, we apply roller boundary conditions at all domain's sides except the top boundary where we apply a uniform normal load $f_N^{top} = 90\,MPa$.

In this study, we examine three fluid physics: single-phase, two-phase two-component and thermal two-phase two-component. Table 4 list parameters which describe single-phase and thermal two-phase fluid physics. For the isothermal two-phase fluid physics, thermal properties should be omitted.

We model the thermo-hydro-mechanical-compositional reservoir response perturbed by the doublet of injection and production wells placed over the longest centerline (along the y-axis) as shown in the top-left of Fig. 13. The vertical wells perforate the whole thickness of the reservoir. Pressure controls $p_{inj} = p_{max} + 50\,bar$ and $p_{prod} = p_{min} - 50\,bar$ are applied to the wells, respectively, where p_{max} and p_{min} are maximal and minimal unperturbed pressures over perforated cells. In all variants of fluid physics, single-phase fluid is pumped into the reservoir through the injection well. In the case of two-phase thermal fluid, specifically, pure water of temperature $\Theta_{inj} = 27.85°C$ is injected. The simulation is performed up to $t_{max} = 20\,d$.

Figs. 14 and 15 demonstrate solution profiles along the longest centerline of the reservoir, indicated by a white line in the top-left of Fig. 13. This centerline passes through the top of the reservoir and is aligned with the y-axis. Fig. 14 presents the vertical displacement and pressure obtained for single-phase fluid while Fig. 15 additionally shows water saturation and water saturation
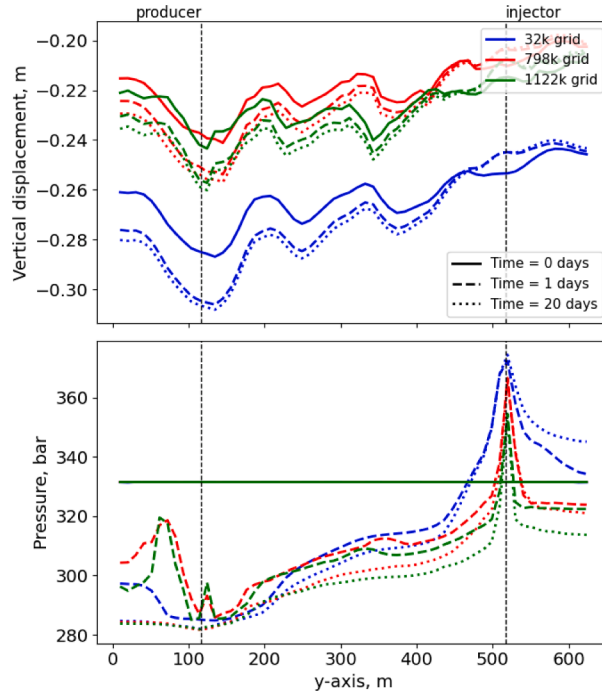
Fig. 14. Solution profiles for single-phase fluid plotted over the longest centerline at the top of the reservoir (white line in the top-left of Fig. 13). The results are displayed for three different grid resolutions and at three time steps.

(a) Two-phase fluid

(b) Thermal two-phase fluid
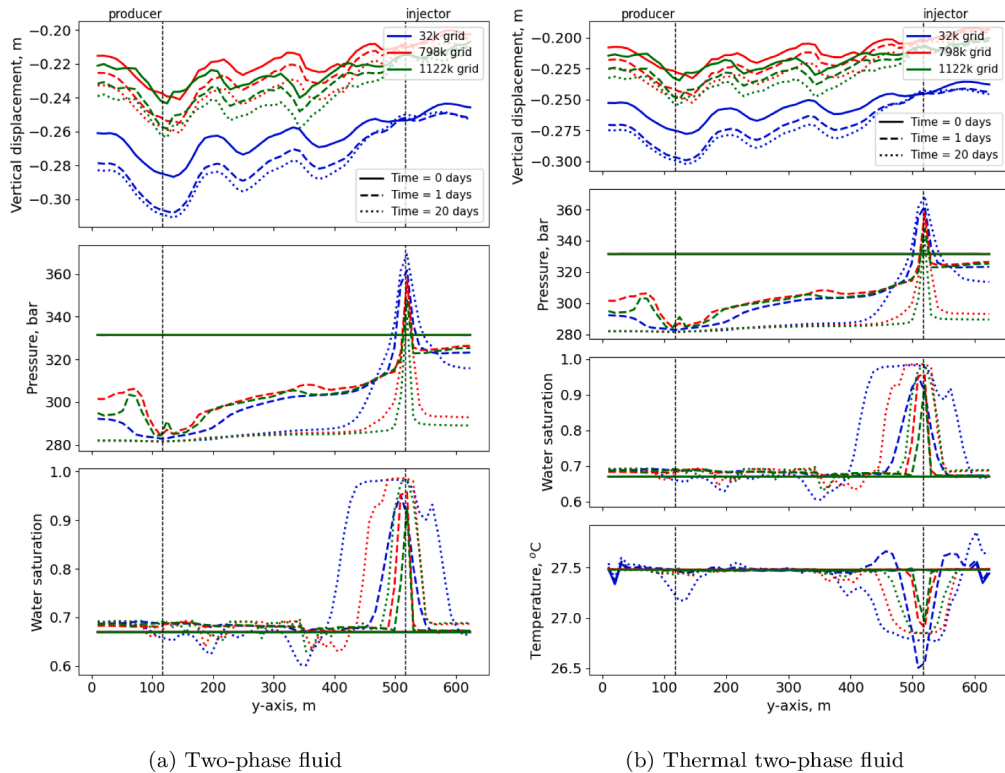
Fig. 15. Solution profiles for two-phase (a) and thermal two-phase (b) fluids plotted over the longest centerline at the top of the reservoir (white line in the top-left of Fig. 13). The results are displayed for three different grid resolutions and at three time steps.
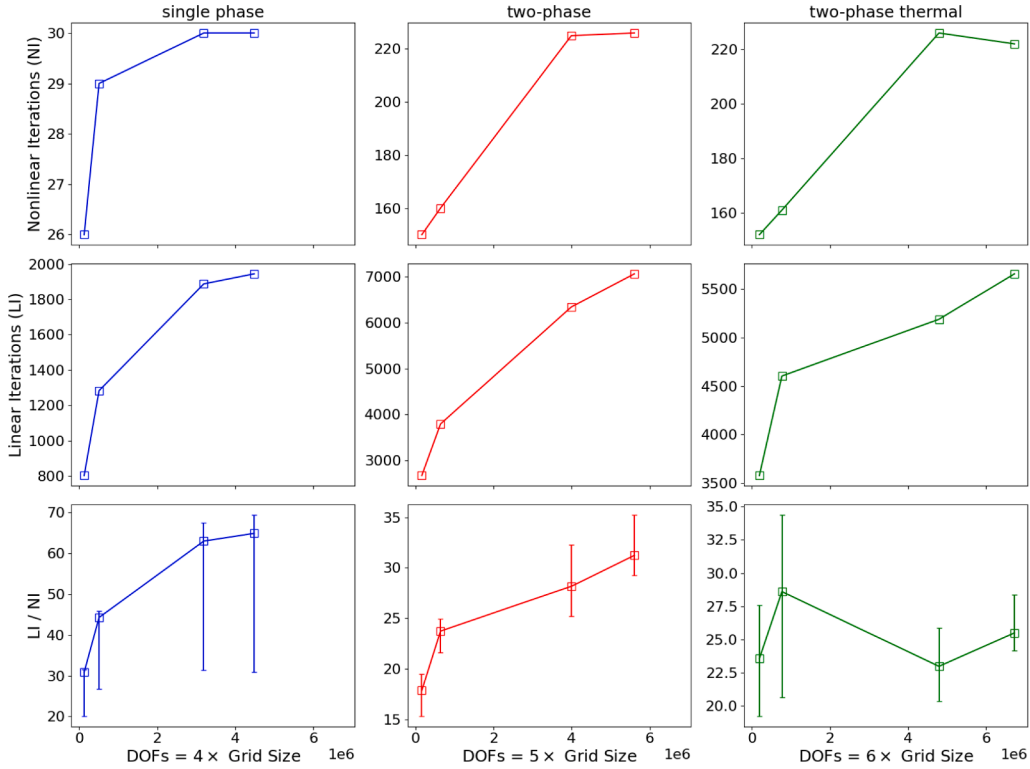
Fig. 16. Scalability study of the block-partitioned preconditioner. The cummulative number of nonlinear iterations (top row), linear iterations (central row) and average number of linear iterations per nonlinear one with deviations (bottom row) in 20 time steps is plotted against number of degrees of freedom (DOFs) in multiple grid resolutions. The results are given for modelling single phase (left column), two-phase (central column) and two-phase thermal (right column) fluid flow.
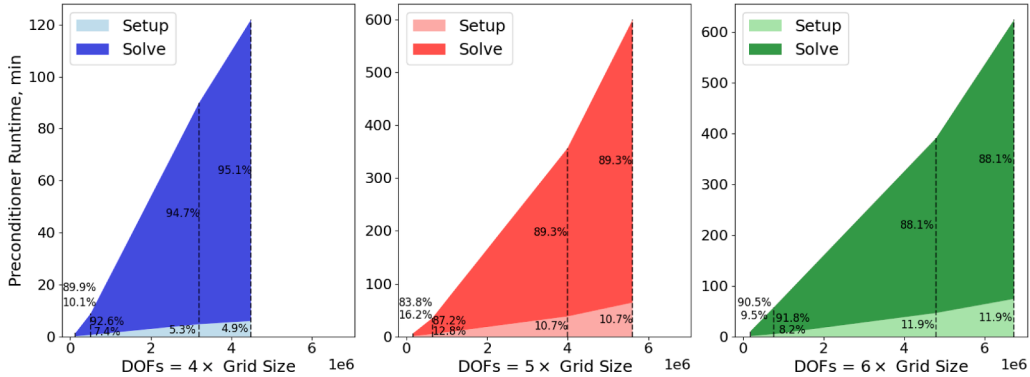

Fig. 17. Cummulative runtime of the block-partitioned preconditioner to achieve convergent solutions in 20 time steps. Timings of setup and solve calls are provided.

with temperature obtained for two-phase and thermal two-phase fluids, respectively. The results for three different grid resolutions and at three time steps $t = 0, 1, 20\,\mathrm{d}$ are shown in both figures.

The vertical displacement profiles for all three fluid types show significant differences between grid resolutions. The results calculated with the coarsest resolution (32k) overestimate vertical displacement compared to those calculated with finer grids. This applies to both the vertical displacement at the initial unperturbed condition ($t = 0\,\mathrm{d}$) and the vertical displacement due to well operation ($t = 20\,\mathrm{d}$). The major contribution to this difference in vertical displacement can be attributed to the varying stiffness heterogeneities specified for different grid resolutions. Additionally, this difference can be partly explained by the difference in pressures obtained for different grid resolutions. Indeed, the pressure spike around the injection well is localized in a narrower region on the finer grids compared to the coarser grid. Besides, the narrower pressure spike around the injection well for finer grids explains the shorter propagation of water saturation and temperature fronts.
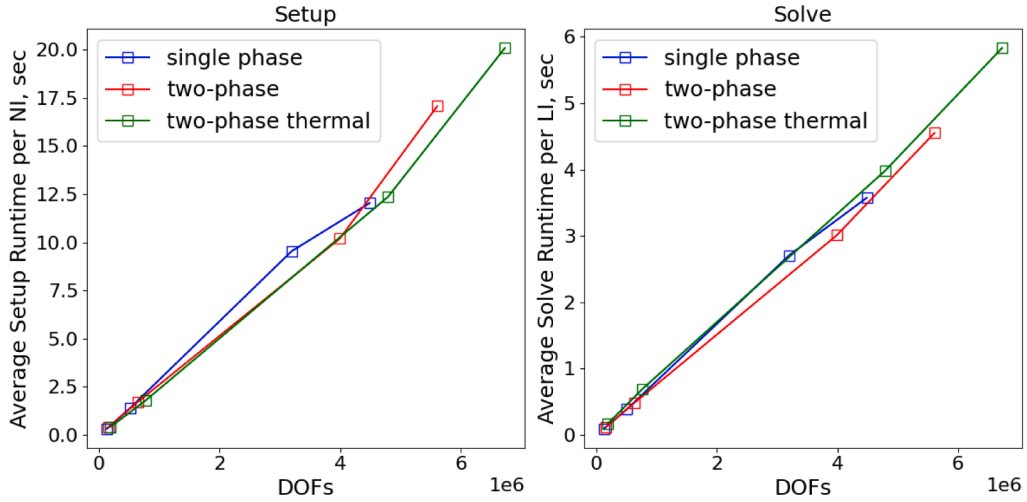
Fig. 18. Average runtime of setup and solve calls per nonlinear (NI) and linear (LI) iteration, respectively, against number of degrees of freedom (DOFs) in various simulation runs.
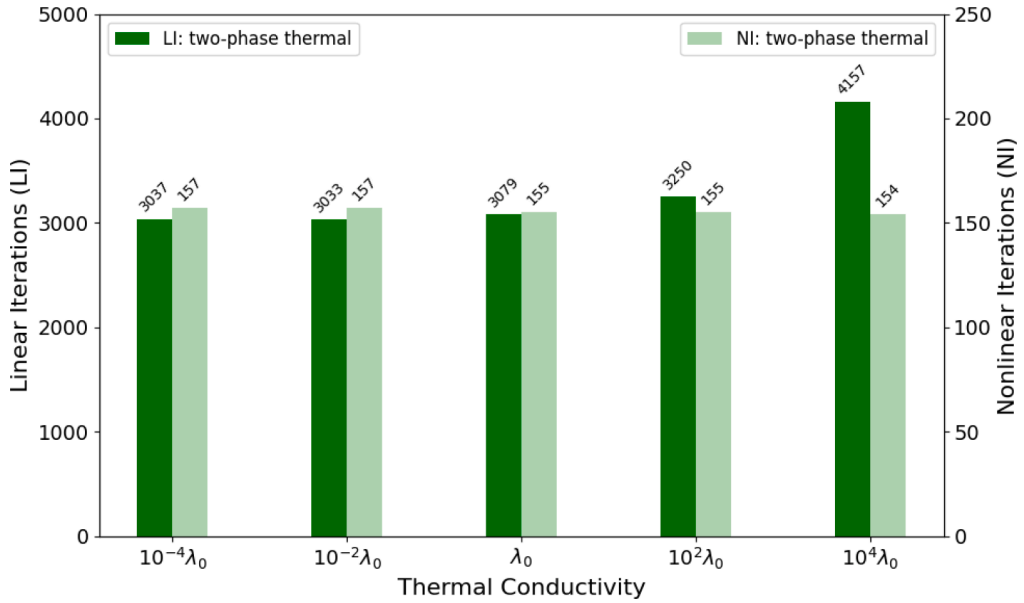
Fig. 19. Sensitivity of linear (left axis) and nonlinear (right axis) iterations to the effective thermal conductivity. Calculations are performed using $24 \times 104 \times 40$ grid with thermal two-phase fluid physics.

Efficient modeling of fully implicitly coupled thermo-hydro-mechanical-compositional processes in realistic settings requires a scalable computational framework. Fig. 16 presents the results of the scalability study of the implemented block-partitioned preconditioner. It shows the number of linear and nonlinear iterations needed to obtain convergent solutions in 20 time steps for various grid resolutions. Moreover, the average numbers of linear iterations per nonlinear iteration are also reported. The model heterogeneities are upscaled from the original SPE10 dataset provided at the finest grid resolution. The results indicate a linear increase in the number of linear iterations with increasing grid size.

For the same model runs, Fig. 17 presents the cummulative runtime of the block-partitioned preconditioner. Additionally, the runtime of the setup and solve calls are specified. The setup call performs the approximation of Schur complement $\tilde{\mathbf{S}}_{\omega}$, including the setup of AMG preconditioners for pressure $\mathbf{J}_{pp}$ and displacement $\mathbf{J}_{uu}$ subsystems every Newton iteration. Note, that under linear thermo-poroelastic assumption and the boundary conditions of the same type, the latter is not needed as $\mathbf{J}_{uu}$ remains constant over iterations and time steps. The solve call performs the solution of flow and, subsequently, displacement subsystems. Although, the setup includes redundant setup of AMG preconditioner for displacement subsystem, it constitutes a small part (<12 %) of preconditioner's runtime. Most of the runtime is taken by solve call, specifically solve of displacement subsystem. The increase in the preconditioner's runtime against grid size is almost linear. Additionally, Fig. 18 present the average runtimes of setup and solve calls per nonlinear

and linear iteration, respectively. Despite different block sizes, the results obtained for different fluids follow almost the same straight line.

Heat conduction terms introduce additional elliptic terms that are not treated efficiently at the CPR stage of the block-partitioned preconditioner. Fig. 19 demonstrates the sensitivity of solving performance to the magnitude of heat conduction term. It shows the number of linear and nonlinear iterations needed to obtain convergent solutions in 20 time steps for multiple values of effective heat conduction coefficient. The figure shows an insignificant increase in linear iterations with higher heat conduction coefficient, for the values of heat conduction between $10^{-4}\lambda_0$ and $10^2\lambda_0$. This almost flat behavior might be explained by an already high number of iterations spent by the block-partitioned preconditioner. In the case of extremely high heat conduction, we observe a significant increase in the number of linear iterations, as anticipated.

4. Conclusion

In this paper, we have introduced a novel cell-centered collocated fully implicit scheme of the Finite Volume Method (FVM) for the coupled modeling of thermo-hydro-mechanical-compositional processes in thermoporoelastic rocks. The scheme benefits from a vectorized form of mass, energy and momentum fluxes using multi-point approximations, that simplifies multiphysical simulation within the FVM framework. Furthermore, the use of collocated FVM for momentum balance enables the natural integration of thermal composition flow with geomechanics within a single computational grid and engine. Additionally, we implemented a block-partitioned preconditioning strategy that alleviates the costs of fully implicit coupling and enables efficient modeling of large realistic setups.

The proposed framework has been validated using a simplified version of the physics which allows us to use an numerical convergence benchmark. We show that in the poroelastic case, the displacements exhibit a nearly quadratic convergence rate while pressure demonstrates a super-linear convergence. In the thermo-poroelastic case, the convergence rate changes from quadratic to lower orders depending on the thermal Peclet number. We also demonstrate how the performance of the full thermo-hydro-mechanical-compositional model depends on the grid resolution using the mechanical extension of the SPE10 model.

Future work would include the development of the robust inf-sup stable extension of the scheme, better tuning of the preconditioner, offloading assembly and solvers to GPU to further minimize computational costs of modeling, and the support of faults with frictional contacts to enable modeling of fault reactivation.

CRediT authorship contribution statement

Aleksei Novikov: Writing – original draft, Software, Methodology, Conceptualization; **Ilshat Saifullin:** Software; **Hadi Hajibeygi:** Writing – review & editing, Methodology; **Denis Voskov:** Writing – review & editing, Supervision, Methodology, Funding acquisition.

Data availability

Data will be made available on request.

Declaration of competing interest

The authors declare that they have no known competing financial interests or personal relationships that could have appeared to influence the work reported in this paper.

Acknowledgements

References

[1] M.D. Zoback, Reservoir Geomechanics, Cambridge University Press, 2007. https://doi.org/10.1017/CBO9780511586477

[2] L. Buijze, Y. Guo, A.R. Niemeijer, S. Ma, C.J. Spiers, Nucleation of stick-slip instability within a large-scale experimental fault: effects of stress heterogeneities due to loading and gouge layer compaction, J. Geophys. Res. 125 (8) (2020), e2019JB018429. https://doi.org/10.1029/2019JB018429

[3] A. Pluymakers, A.G. Muntendam-Bos, A. Niemeijer, Induced seismicity: a global phenomenon with special relevance to the Dutch subsurface, Neth. J. Geosci. 102 (2023). https://doi.org/10.1017/njg.2023.2

[4] W.L. Ellsworth, D. Giardini, J. Townend, S. Ge, T. Shimamoto, Triggering of the Pohang, Korea, earthquake (Mw 5.5) by enhanced geothermal system stimulation, Seismol. Res. Lett. 90 (5) (2019) 1844–1858. https://doi.org/10.1785/0220190102

[5] R. Schultz, A. Muntendam-Bos, W. Zhou, G.C. Beroza, W.L. Ellsworth, Induced seismicity red-light thresholds for enhanced geothermal prospects in the Netherlands, Geothermics 106s (2022) 102580. https://doi.org/10.1016/j.geothermics.2022.102580

[6] J. Rohmer, A. Pluymakers, F. Renard, Mechano-chemical interactions in sedimentary rocks in the context of CO2 storage: weak acid, weak effects?, Earth-Science Rev. 157 (2016) 86–110. https://doi.org/10.1016/j.earscirev.2016.03.009

[7] Y. Cheng, W. Liu, T. Xu, Y. Zhang, X. Zhang, Y. Xing, B. Feng, Y. Xia, Seismicity induced by geological CO2 storage: a review, Earth-Science Rev. 239 (2023). https://doi.org/10.1016/j.earscirev.2023.104369

[8] R. Deb, P. Jenny, Finite volume-based modeling of flow-induced shear failure along fracture manifolds, Int. J. Numer. Anal. Methods Geomech. 41 (18) (2017) 1922–1942. https://doi.org/10.1002/nag.2707

[9] I. Sokolova, M.G. Bastisya, H. Hajibeygi, Multiscale finite volume method for finite-volume-based simulation of poroelasticity, J. Comput. Phys. 379 (2019) 309–324. https://doi.org/10.1016/j.jcp.2018.11.039

[10] S. Shokrollahzadeh Behbahani, H. Hajibeygi, D.V. Voskov, J.D. Jansen, Smoothed embedded finite-volume method (sEFVM) for modeling contact mechanics in deformable faulted and fractured porous media, J. Comput. Phys. (2022). https://doi.org/{10.1016/j.jcp.2022.111143}.

[11] J.M. Nordbotten, Cell-centered finite volume discretizations for deformable porous media, Int. J. Numer. Methods Eng. 100 (6) (2014) 399–418. https://doi.org/10.1002/nme.4734

[12] K.M. Terekhov, H.A. Tchelepi, Cell-centered finite-volume method for elastic deformation of heterogeneous media with full-tensor properties, J. Comput. Appl. Math. 364 (2020), 112331. https://doi.org/10.1016/j.cam.2019.06.047

[13] A. Novikov, D. Voskov, M. Khait, H. Hajibeygi, J.D. Jansen, A scalable collocated finite volume scheme for simulation of induced fault slip, J. Comput. Phys. 469 (2022). https://doi.org/10.1016/j.jcp.2022.111598

[14] I. Demiredzic, D. Martinovic, A. Ivankovic, Numerical simulation of thermal deformation in welded workpiece; [Numericka simulacija termodeformacionih procesa u zavarenom komadu], Zavarivanje 31 (5–6) (1988) 209–219. https://www.scopus.com/inward/record.uri?eid = 2-s2.0-0024180048&partnerID = 40&md5 = 49392edde55d2780bd8e4b8a350fbafb.

[15] E. Keilegavlen, J.M. Nordbotten, Finite volume methods for elasticity with weak symmetry, Int. J. Numer. Methods Eng. 112 (8) (2017) 939–962. https://doi.org/10.1002/nme.5538

[16] K.M. Terekhov, Cell-centered finite-volume method for heterogeneous anisotropic poromechanics problem, J. Comput. Appl. Math. 365 (2020), 112357. https://doi.org/10.1016/j.cam.2019.112357

[17] K.M. Terekhov, Collocated inite-volume method for the incompressible navier-stokes problem, J. Numer. Math. 29 (1) (2021) 63–79. https://doi.org/10.1515/jnma-2020-0008

[18] R. Deb, P. Jenny, Modeling of shear failure in fractured reservoirs with a porous matrix, Comput. Geosci. 21 (5–6) (2017) 1119–1134. https://doi.org/10.1007/s10596-017-9680-x

[19] T.T. Garipov, P. Tomin, R. Rin, D.V. Voskov, H.A. Tchelepi, Unified thermo-compositional-mechanical framework for reservoir simulation, Comput. Geosci. 22 (4) (2018) 1039–1057. https://doi.org/10.1007/s10596-018-9737-5

[20] A. Settari, F.M. Mourits, A coupled reservoir and geomechanical simulation system, SPE J. 3 (3) (1998) 219–226. https://doi.org/10.2118/50939-PA

[21] J. Kim, H.A. Tchelepi, R. Juanes, Stability and convergence of sequential methods for coupled flow and geomechanics: fixed-stress and fixed-strain splits, Comput. Methods Appl. Mech. Eng. 200 (13–16) (2011) 1591–1606. https://doi.org/10.1016/j.cma.2010.12.022

[22] T.T. Garipov, M. Karimi-Fard, H.A. Tchelepi, Discrete fracture model for coupled flow and geomechanics, Comput. Geosci. 20 (1) (2016) 149–160. https://doi.org/10.1007/s10596-015-9554-z

[23] J.A. White, N. Castelletto, S. Klevtsov, Q.M. Bui, D. Osei-Kuffuor, H.A. Tchelepi, A two-stage preconditioner for multiphase poromechanics in reservoir simulation, Comput. Methods Appl. Mech. Eng. 357 (2019). https://doi.org/10.1016/j.cma.2019.112575

[24] O.A. Ladyzhenskaya, The Mathematical Theory of Viscous Incompressible Flow, Gordon & Breach (1969).

[25] M.F. Franco Brezzi, Mixed and Hybrid Finite Element Methods, Springer Series in Computational Mathematics, Springer, first ed., 1991.

[26] M.A. Murad, A.F.D. Loula, On stability and convergence of finite element approximations of Biot's consolidation problem, Int. J. Numer. Methods Eng. 37 (4) (1994) 645–667. https://doi.org/10.1002/nme.1620370407

[27] F.J. Gaspar, F.J. Lisbona, C.W. Oosterlee, A stabilized difference scheme for deformable porous media and its numerical resolution by multigrid methods, Comput. Vis. Sci. 11 (2) (2008) 67–76. https://doi.org/10.1007/s00791-007-0061-1

[28] M. Ferronato, N. Castelletto, G. Gambolati, A fully coupled 3-D mixed finite element model of biot consolidation, J. Comput. Phys. 229 (12) (2010) 4813–4830. https://doi.org/10.1016/j.jcp.2010.03.018

[29] M. Preisig, J.H. Prévost, Stabilization procedures in coupled poromechanics problems: a critical assessment, Int. J. Numer. Anal. Methods Geomech. 35 (11) (2011) 1207–1225. https://doi.org/10.1002/nag.951

[30] J.M. Nordbotten, Stable cell-centered finite volume discretization for biot equations, SIAM J. Numer. Anal. 54 (2) (2016) 942–968. https://doi.org/10.1137/15M1014280

[31] K.M. Terekhov, Y.V. Vassilevski, Finite volume method for coupled subsurface flow problems, II: poroelasticity, J. Comput. Phys. 462 (2022). https://doi.org/10.1016/j.jcp.2022.111225

[32] A. Novikov, A Finite Volume Framework for Accurate Modeling of Fault Reactivation in Poroelastic Rocks, Dissertation (tu delft), Delft University of Technology, 2024. https://doi.org/10.4233/uuid:1f4731b3-cbdd-4317-98f7-8520b7446684

[33] J.A. White, N. Castelletto, H.A. Tchelepi, Block-partitioned solvers for coupled poromechanics: a unified framework, Comput. Methods Appl. Mech. Eng. 303 (2016) 55–74. https://doi.org/10.1016/j.cma.2016.01.008

[34] S. Klevtsov, N. Castelletto, J.A. White, H.A. Tchelepi, Block-preconditioned krylov methods for coupled multiphase reservoir flow and geomechanics, 15th European Conference on the Mathematics of Oil Recovery, ECMOR 2016 (2016). https://doi.org/10.3997/2214-4609.201601900

[35] M. Khait, D.V. Voskov, Operator-based linearization for general purpose reservoir simulation, J. Pet. Sci. Eng. 157 (2017) 990–998. https://doi.org/10.1016/j.petrol.2017.08.009

[36] D. Voskov, I. Saifullin, A. Novikov, M. Wapperom, L. Orozco, G.S. Seabra, Y. Chen, M. Khait, X. Lyu, X. Tian, S. de Hoop, A. Palha, Open delft advanced research terra simulator (open-DARTS), J. Open Source Softw. 9 (99) (2024) 6737. https://doi.org/10.21105/joss.06737

[37] M. Khait, D. Voskov, Adaptive parameterization for solving of thermal/compositional nonlinear flow and transport with buoyancy, SPE J. 23 (2) (2018) 522–534. https://doi.org/10.2118/182685-pa

[38] X. Lyu, M. Khait, D. Voskov, Operator-based linearization approach for modeling of multiphase flow with buoyancy and capillarity, SPE J. 26 (4) (2021) 1858–1878. https://doi.org/10.2118/205378-PA

[39] M. Khait, D. Voskov, Operator-based linearization for efficient modeling of geothermal processes, Geothermics 74 (2018) 7–18. https://doi.org/10.1016/j.geothermics.2018.01.012

[40] Y. Wang, D. Voskov, M. Khait, D. Bruhn, An efficient numerical simulator for geothermal simulation: a benchmark study, Appl. Energy 264 (2020). https://doi.org/10.1016/j.apenergy.2020.114693

[41] K. Kala, D. Voskov, Element balance formulation in reactive compositional flow and transport with parameterization technique, Comput. Geosci. 24 (2) (2020) 609–624. https://doi.org/10.1007/s10596-019-9828-y

[42] X. Lyu, D. Voskov, W.R. Rossen, Numerical investigations of foam-assisted CO2 storage in saline aquifers, Int. J. Greenh. Gas Control 108 (2021), 103314. https://doi.org/10.1016/j.ijggc.2021.103314

[43] O. Coussy, Thermoporoelasticity, John Wiley & Sons, Ltd, 2003, pp. 71–112. https://doi.org/10.1002/0470092718.ch4

[44] Y. Zhao, R.I. Borja, A continuum framework for coupled solid deformation-fluid flow through anisotropic elastoplastic porous media, Comput. Methods Appl. Mech. Eng. 369 (2020), 113225. https://doi.org/10.1016/j.cma.2020.113225

[45] M. Wapperom, X. Lyu, D.V. Nichita, D. Voskov, A unified thermal-reactive compositional simulation framework for modeling CO_2 sequestration at various scales, Society of Petroleum Engineers - SPE Reservoir Simulation Conference, RSC 2023 (2023). https://doi.org/10.2118/212182-MS

[46] A.H.D. Cheng, Material coefficients of anisotropic poroelasticity, Int. J. Rock Mech. Min. Sci. Geomech. Abstr. 34 (2) (1997) 199–205. https://doi.org/10.1016/S0148-9062(96)00055-1

[47] M.L. Michelsen, The isothermal flash problem. Part II. Phase-split calculation, Fluid Phase Equilib. 9 (1) (1982) 21–40. https://doi.org/10.1016/0378-3812(82)85002-4

[48] J.M. Nordbotten, W.M. Boon, O. Duran, E. Keilegavlen, Mixed finite element and TPSA finite volume methods for linearized elasticity and cosserat materials, 19th European Conference on the Mathematics of Geological Reservoirs, ECMOR 2024 2024 (1) (2024) 1–12. https://doi.org/10.3997/2214-4609.202437014

[49] I. Aavatsmark, T. Barkve, O. Boe, T. Mannseth, Discretization on non-orthogonal, quadrilateral grids for inhomogeneous, anisotropic media, J. Comput. Phys. 127 (1) (1996) 2–14. https://doi.org/10.1006/jcph.1996.0154

[50] M.G. Edwards, C.F. Rogers, Finite volume discretization with imposed flux continuity for the general tensor pressure equation, Comput. Geosci. 2 (1998) 259–290. https://doi.org/10.1023/A:1011510505406

[51] E. Keilegavlen, I. Aavatsmark, Monotonicity for control volume methods on unstructured grids, ECMOR 2008 - 11th European Conference on the Mathematics of Oil Recovery (2008). https://doi.org/10.3997/2214-4609.20146378

[52] I. Stefansson, I. Berre, E. Keilegavlen, Finite volume discretisation of fracture deformation in thermo-poroelastic media, Springer Proc. Math. Stat. 323 (2020) 519–526. https://doi.org/10.1007/978-3-030-43651-348

[53] I. Stefansson, I. Berre, E. Keilegavlen, A fully coupled numerical model of thermo-hydro-mechanical processes and fracture contact mechanics in porous media, Comput. Methods Appl. Mech. Eng. 386 (2021) 114122. https://doi.org/10.1016/j.cma.2021.114122

[54] M. Schneider, D. Gläser, B. Flemisch, R. Helmig, Comparison of finite-volume schemes for diffusion problems, Oil as Sci. Technol. 73 (1) (2018). https://doi.org/10.2516/ogst/2018064

[55] C. Le Potier, Finite volume monotone scheme for highly anisotropic diffusion operators on unstructured triangular meshes; [Schéma volumes finis monotone pour des opérateurs de diffusion fortement anisotropes sur des maillages de triangles non structurés], C.R. Math. 341 (12) (2005) 787–792. https://doi.org/10.1016/j.crma.2005.10.010

[56] K.M. Terekhov, B.T. Mallison, H.A. Tchelepi, Cell-centered nonlinear finite-volume methods for the heterogeneous anisotropic diffusion problem, J. Comput. Phys. 330 (2017) 245–267. https://doi.org/10.1016/j.jcp.2016.11.010

[57] S.R.T. Tripuraneni, A. Novikov, D. Voskov, Nonlinear finite volume discretization of geomechanical problem, Int. J. Numer. Anal. Methods Geomech. 47 (12) (2023) 2283–2303. https://doi.org/10.1002/nag.3580

[58] G. Manzini, M. Putti, Mesh locking effects in the finite volume solution of 2-D anisotropic diffusion equations, J. Comput. Phys. 220 (2) (2007) 751–771. https://doi.org/10.1016/j.jcp.2006.05.026

[59] D.V. Voskov, Operator-based linearization approach for modeling of multiphase multi-component flow in porous media, J. Comput. Phys. 337 (2017) 275–288. https://doi.org/10.1016/j.jcp.2017.02.041

[60] M. Wapperom, D. Voskov, J. Heringer, Open DARTS-flash, 2024. https://doi.org/10.5281/zenodo.12686021

[61] Y. Saad, Iterative Methods for Pparse Linear Systems, Society for Industrial and Applied Mathematics, second ed., 2003. https://doi.org/10.1137/1.9780898718003

[62] J.H. Bramble, D.Y. Kwak, J.E. Pasciak, Uniform convergence of multigrid V-cycle iterations for indefinite and nonsymmetric problems, SIAM J. Numer. Anal. 31 (6) (1994) 1746–1763. https://doi.org/10.1137/0731089

[63] Z. Chen, D.Y. Kwak, Y.J. Yon, Multigrid algorithms for nonconforming and mixed methods for nonsymmetric and indefinite problems, SIAM J. Sci. Comput. 19 (2) (1998) 502–515. https://doi.org/10.1137/S1064827595289790

[64] T. Clees, AMG Strategies for PDE Systems with Applications in Industrial Semiconductor Simulation, Ph.D. thesis, University of Cologne, 2005.

[65] J. Gopalakrishnan, J.E. Pasciak, L.F. Demkowicz, Analysis of a multigrid algorithm for time harmonic maxwell equations, SIAM J. Numer. Anal. 42 (1) (2004) 90–108. https://doi.org/10.1137/S003614290139490X

[66] S. Gries, On the convergence of system-AMG in reservoir simulation, SPE J. 23 (02) (2018) 589–597. https://onepetro.org/SJ/article-pdf/23/02/589/2114383/spe-182630-pa.pdf, https://doi.org/10.2118/182630-PA

[67] S. Gries, B. Metsch, K.M. Terekhov, P. Tomin, System-AMG for fully coupled reservoir simulation with geomechanics, Society of Petroleum Engineers - SPE Reservoir Simulation Conference 2019, RSC 2019 (2019). https://doi.org/10.2118/193887-ms

[68] I. Aavatsmark, G.T. Eigestad, R.A. Klausen, M.F. Wheeler, I. Yotov, Convergence of a symmetric MPFA method on quadrilateral grids, Comput. Geosci. 11 (4) (2007) 333–345. https://doi.org/10.1007/s10596-007-9056-8

[69] H.A. Friis, M.G. Edwards, J. Mykkeltveit, Symmetric positive definite flux-continuous full-tensor finite-volume scheme s on unstructured cell-centered triangular grids, SIAM J. Sci. Comput. 31 (2) (2008) 1192–1220. https://doi.org/10.1137/070692182

[70] F. Bertrand, Z. Cai, E.Y. Park, Least-squares methods for elasticity and stokes equations with weakly imposed symmetry, Comput. Methods Appl. Math. 19 (3) (2019) 415–430. https://doi.org/10.1515/cmam-2018-0255

[71] K.M. Terekhov, Y.V. Vassilevski, Finite volume method for coupled subsurface flow problems, I: darcy problem, J. Comput. Phys. 395 (2019) 298–306. https://doi.org/10.1016/j.jcp.2019.06.009

[72] J.R. Wallis, R.P. Kendall, T.E. Little, Constrained residual acceleration of conjugate residual methods, Society of Petroleum Engineers of AIME, (Paper) SPE (1985) 415–428. https://doi.org/10.2523/13536-ms

[73] H. Cao, H.A. Tchelepi, J. Wallis, H. Yardumian, Parallel scalable unstructured CPR-type linear solver for reservoir simulation, Proceedings - SPE Annual Technical Conference and Exhibition (2005) 3319–3326. https://doi.org/10.2523/96809-ms

[74] K.A. A. Settari, Petroleum Reservoir Simulation, Applied Science Publishers LTD, 1979.

[75] M. Khait, D. Voskov, R. Zaydullin, High performance framework for modelling of complex subsurface flow and transport applications, ECMOR 2020 - 17th European Conference on the Mathematics of Oil Recovery (2020). https://doi.org/10.3997/2214-4609.202035188

[76] T. Roy, T.B. Jonsthovel, C. Lemon, A.J. Wathen, A constrained pressure-temperature residual (CPTR) method for non-isothermal multiphase flow in porous media, SIAM J. Sci. Comput. 42 (4) (2020) B1014–B1040. https://doi.org/10.1137/19M1292023

[77] M.A. Cremon, J. Franc, F.P. Hamon, Constrained pressure-temperature residual (CPTR) preconditioner performance for large-scale thermal CO2 injection simulation, Comput. Geosci. (2024). https://doi.org/10.1007/s10596-024-10292-z

[78] V.E. Henson, U.M. Yang, BoomerAMG: a parallel algebraic multigrid solver and preconditioner, Appl. Numer. Math. 41 (1) (2002) 155–177. https://doi.org/10.1016/S0168-9274(01)00115-5

[79] A. Verruijt, Theory and Problems of Poroelasticity, Delft University Press, 2016. https://geo.verruijt.net.

[80] R.M. Aronson, N. Castelletto, F.P. Hamon, J.A. White, H.A. Tchelepi, Pressure-stabilized fixed-stress iterative solutions of compositional poromechanics, Comput. Methods Appl. Mech. Eng. 427 (2024). https://doi.org/10.1016/j.cma.2024.117008

[81] Q. Gao, A. Ghassemi, Three-dimensional thermo-poroelastic modeling and analysis of flow, heat transport and deformation in fractured rock with applications to a lab-scale geothermal system, Rock Mech. Rock Eng. 53 (2020) 1–22. https://doi.org/10.1007/s00603-019-01989-0

[82] B. Bai, One-dimensional thermal consolidation characteristics of geotechnical media under non-isothermal condition, Gongcheng Lixue/Eng. Mech. 22 (2005) 186–191.